THESIS FOR THE DEGREE OF LICENTIATE OF ENGINEERING

Interpolymer complexation of a polymer brush

John Andersson

Department of Chemistry and Chemical Engineering
Division of Applied chemistry
Chalmers University of Technology
Gothenburg, Sweden, 2020

Interpolymer complexation of a polymer brush

John Andersson

Cover image: The height of a polymer brush layer (green strings) changes when a second interactive polymer (purple strings) binds to it at low pH and rinses off again as pH is changed back. The same interaction mechanism could potentially be applied to functionalised nanostructures to open and close paths blocked by the polymer brush.

Licentiatuppsatser vid Institutionen för kemi och kemiteknik
Chalmers tekniska högskola.
No. 2020:18

Department of Chemistry and Chemical Engineering
Chalmers University of Technology
SE-412 96 Gothenburg, Sweden
Phone: +46 (0)31 772 1000
www.chalmers.se

Supervisor: Andreas Dahlin
Examinor: Martin Andersson

Printed by Chalmers Reproservice
Gothenburg, Sweden, November 2020

Interpolymer complexation of a polymer brush

John Andersson
Chemistry and Chemical Engineering
Chalmers University of Technology

Abstract

Controllable macromolecular gating between nanoscopic compartments is of high interest for single molecule studies of biological macromolecules. By definition, a good macromolecular gate should completely stop biomolecules, such as proteins, from crossing between compartments in its closed state while letting them pass in its open state. Polymer brushes of poly(ethylene glycol) have been proven excellent barriers for proteins in previous work, but are limited in terms of stimuli-responsive behaviour needed for macromolecular gating. In this thesis work, the pH reversible interpolymer complexation between a poly(ethylene glycol) brush and poly(methacrylic acid) was investigated as a potential macromolecular gating mechanism. Conclusions were based on the evaluation of the resulting surface complex using three surface sensitive characterisation techniques. Upon complexing at low pH, the polymer layer was found to adopt a shrunken state with significant behavioural changes, while completely reversing back to its initial state after a neutral pH had been introduced. This pH reversible interaction show great promise as a pH controlled macromolecular gating mechanism and calls for further studies with suitable nanostructures. To this end, the fabrication and properties of a new solid-state nanopore device is also presented, together with the direction needed for future work towards a new macromolecular gating system.

Keywords: Interpolymer complex, polymer brush, pH responsive, nanopores, functional materials, macromolecular gating.

List of Publications

This thesis is based on the following publications:

Paper 1:
Control of polymer brush morphology, rheology and protein repulsion by hydrogen bond complexation.
John Andersson, Gustav Ferrand-Drake del Castillo, Pierluigi Bilotto, Fredrik Höök and Andreas Dahlin
Manuscript to be submitted to Macromolecules.

Author contribution:
Performed all experiments and analysis, except for sample preparations, measurements and analysis of the SFA experiment. Co-authored the manuscript.

Paper 2:
Optical properties of plasmonic nanopore arrays prepared by electron beam and colloidal lithography.
Bita Malekian, Kunli Xiong, Evan S. H. Kang, **John Andersson**, Gustav Emilsson, Marcus Rommel, Takumi Sannomiya, Magnus P. Jonsson, and Andreas Dahlin
Published in Nanoscale Advances, Oct. 2019, pp. 4282—4289

Author contribution:
Performed part of the nanopore membrane fabrication. Co-authored the manuscript.

Acknowledgements

First of all, my sincere thanks to the Erling-Persson Family Foundation for financially supporting this work. I would then like to thank my supervisor Andreas for all his help, teachings, and patience both for what has been but also what is to come. I would like to thank all the great colleagues of my group (in no particular order): Gustav, Rebekah, Justas, Jolie, Marika, Oliver, Bita, Kunli, Tim, Sophia, Gustav, Asaad and Zeynep for additional help, great lunches and the fun times in and out of the lab! My thanks also to all other colleagues here at the division of Applied surface chemistry which make work fun and exciting, the SFA gang over in Vienna for the great collaboration, friends and family for all support, my cats Stina and Siri for their fluffy distractions when writing (Figure 0.1) and last, but not least, Linnea for her endless love and support in all I do no matter the stupidity involved...

All the best,
John, November 2020, Sandsbacka

Figure 0.1: Components of the writing setup, including fluffy distractions.

Contents

CHAPTER 1

Introduction

Life is a fascinating concept and likely among the most intricate phenomena in our universe. In the field of biology, researchers study the behaviour and origins of life at a macrological scale and since the early 18th century starting with Carl von Linné, "the father of taxonomy", biologists have meticulously characterised fauna from all over the world by identifying different species and categorising their parts. In more recent times, scientists within molecular biology have continued with this approach also for life's basic molecular components: carbohydrates, lipids, nucleic acids, and in particular, the molecular building blocks of life known as proteins. As of November 2020, over 195 000 000[1] potential protein variants have been identified, out of which only around 170 000 or 0.1 %[2] have had their three dimensional molecular structure determined. Based on these figures it is clear that we have only scratched the tip of an iceberg of knowledge thus far and still have a long way to go in discovering all components supporting the complexity of life.

As if the sheer number of components was not enough, molecular biologists now agree that biological molecules can exist in different states that each may affect their interaction with other molecules and can change a protein's functionality, which in turn may have significant effects for biological processes. Within one class of proteins categorised as Intrinsically disorder proteins (IDPs), this structurally dynamic molecular behaviour is particularly prevalent and dictates their main functionality[3]. Their relevance cannot be understated, since IDPs have been identified as the cause of many types of diseases due to various "mis-behaviours" (misfolding, misidentification, missignaling etc.)[4]. However, protein dynamics is not the sole motivator for single-biomolecule studies, because conventional ensemble averaging measurements can also obscure things, such as rare sub-populations, intermediary configurations or multiple reactionary pathways[5]. Thus, in order to further our molecular understanding of life, we need to better understand the roles of the different states of individual biomolecules and how they affect biological processes on the smallest possible scales.

Getting there means we need tools that can study the interactions and dynamics at single-molecule resolution. The tools must also be gentle enough as to not adversely affect the states of the molecules as they are studied, or else we might misinterpret their behaviour as a result. Therefore, one may think of our end goal as to avoid the analogous situation of interrogating a chained biomolecule with a sharp stick in a torture chamber, and instead create a biomolecular living room where the molecule can sit back and feel at home while it's politely asked a few questions over a cup of tea. The problems left to solve for realising single-molecule studies essentially boil down to that of *observation* and *non-intrusive entrapment*. Luckily, the observation problem has mostly been solved by many newly emerging super-resolution techniques[6]. However, while the most common entrapment techniques, such as optical tweezers[7], can keep proteins in place long enough for observation, they cannot be considered non-intrusive due to strong field gradients and requiring a tether to a larger particle.

To solve the problem of non-intrusive entrapment, we should take a few steps back and again consider the natural environment of biomolecules: the tiny but crowded compartments and organelles inside our cells. The size of these compartments are well within the reach of what modern nanotechnology can

readily replicate with established nanofabrication techniques of solid-state materials[7]. For example, a solid-state nanopore (essentially a nano-sized hole between two compartments) is a good geometrical basis for biomimetic molecular compartments, but in order to make nanopores more generally applicable with single-biomolecule studies they need to be modified with additional functionality. Fortunately, several types of surface coatings and functionalisation strategies can be applied to solid-state nanopores to provide this[8]. While passive selective surface functionalisations that mimic the regulated biomolecular transport similar to the nuclear pore complex inside our cells could be one solution[9], having an actively controlled biomolecule translocation system could prove even more useful for single-molecule studies. Essentially, what we are looking for is a macromolecular gating system that can be triggered on demand and applied to solid-state nanopores.

A macromolecular gating system requires a "door", i.e. something which can block larger biomolecules while still letting solvent and small molecules through, but also be opened with respect to the biomolecules by some external stimuli. This leads us into the field of materials undergoing conformational or phase changes depending on environmental factors, often referred to as stimuli-responsive materials in the literature[10]. That being said, materials which are known to effectively repel biomolecules could perhaps be a better starting point since this should be the default state. For example, polymer brushes of poly(ethylene glycol) (PEG) have been studied as protein repelling coatings on drug delivery vehicles for a long time[11] and recent work from our research group demonstrated how they also can effectively block protein translocation in nanopores[12]. While PEG brushes cannot be considered stimuli-responsive in themselves (other than at very poor solvent conditions[13]), there are examples in the literature of pH sensitive interactions between PEG and poly(carboxylic acids) forming interpolymer complexes in solution[14].

In this thesis work, the morphological and rheological behaviour of PEG brushes interacting with poly(methacrylic acid) in solution at low pH has been thoroughly investigated in order to evaluate its potential as a macromolecular gating system. The characterisation was performed using surface sensitive techniques including Surface plasmon resonance, Quartz-crystal microbalance with dissipation monitoring and a Surface force apparatus. Extensive theory

sections are also provided to aid the interested reader in fully understanding the presented experiments. Finally, the fabrication and properties of a new plasmonic nanopore array is presented along with its role in realising a non-intrusive single-molecule entrapment system in future work.

CHAPTER 2

Polymer theory

The work presented in this thesis is largely based on the use of polymers in solution. Polymers are simply defined as macromolecules consisting of a large number of covalently bound monomeric repeat units. The following sections aim to provide an understanding of the concepts relevant for how dissolved polymers behave free in solution and when grafted to surfaces, as well as the unique properties of the particular polymers used throughout this work.

2.1 Polymers in solution

Firstly, the topic of polymers is vast and there is a wide variety of types of polymers that possess an equally vast range of properties. Here we restrict ourselves to what can be considered linear polymers dissolved in solution, where the volume fraction of polymer is much less than that of the solvent molecules themselves. Since fully simulating the interactions and behaviours of all polymers in a solvent breaks down to a many-body problem, the best we can do is to look at an approximated system with a reduced dimensionality.

A great deal of activity within this field occurred around the mid 20th century, which eventually ended up leading to a nobel prize in chemistry 1974 to Paul J. Flory for what is now known as the Flory theory of polymer chains. In his mean-field theory, a polymer chain in solution can be considered as an entropic spring, where the more stretched a polymer chain is, the more it will try to contract in order to increase its entropy and minimize its free energy[15], [16]. Due to each monomer occupying a certain volume, there must simultaneously exist a balancing force which prevent the polymer and its monomers to overlap, thus acting radially outwards from the center of the polymer coil. This balancing force can be thought of in terms of osmotic pressure or entropic forces. The monomer volume which cannot be occupied by anything else is known as the exclusion volume.

Flory also recognised that the properties of the solvent will play a role in the effective exclusion volume of the polymer chain and thus derived different descriptions depending on if the solvent interactions with the polymer could be considered favourable or unfavourable. The total Gibb's free energy for a polymer coil in solution including the conformational entropy, excluded volume and solvent interaction terms can be written as[17]:

$$G(r) = \frac{3k_BTr^2}{2abN} + \frac{k_BTvN^2}{r^3}\left[1 - \chi\right] + C \tag{2.1}$$

where r is the radius of the polymer coil, k_B is Boltzmann's constant, T is temperature, N is the number of monomer units (degree of polymerization), a is the monomer size, b is the Kuhn length (effectively a measure of chain

stiffness), v is the exclusion volume, C is a constant and χ is the dimensionless solvency parameter, which can be expressed along the lines of:

$$\chi = \frac{z}{2k_BT}\left[2\epsilon_{ps} - \epsilon_{ss} - \epsilon_{pp}\right] \tag{2.2}$$

where z is the number of contact points, $\epsilon_{ps}, \epsilon_{ss}, \epsilon_{pp}$ are the interaction energies of the polymer-solvent, solvent-solvent and polymer-polymer interactions respectively. Note that the interaction energies are in the form of energy barriers, where favourable interactions decrease the energy ($\downarrow \epsilon$). It is also worth mentioning that finding accurate values for the physical polymer chain parameters a, b, v and especially the interaction energies (which depend on environmental conditions such as temperature, ionic strength, pH etc.) is no trivial task. Because it is difficult to determine the solvency parameter χ in practice, it is commonly factored into the excluded volume parameter v, which then becomes dependent on solvent properties.

If we minimize the free energy with respect to r by taking the derivative equal to 0, we can find the most probable polymer coil size:

$$\frac{\partial G}{\partial r} = \frac{3k_BTr}{abN} + \frac{3k_BTvN^2}{r^4}\left[1 - \chi\right] = 0 \tag{2.3}$$

$$r = (abv[1-\chi])^{1/5}N^{3/5} \tag{2.4}$$

Note that the coil size scales most strongly with the degree of polymerization (and thus with the average molecular weight of the polymer chains), but still the monomer geometry, chain stiffness and solvent interactions play an important role.

As can be seen in equation 2.2 and 2.4, higher polymer-solvent interaction will tend to stretch out the polymer coil, while the opposite is true for strong solvent-solvent or polymer-polymer interactions. For conditions where $\chi \to 1$, the solvent interaction counteract the excluded volume effect and the polymer will behave just like an ideal chain exhibiting a random walk behaviour. The polymer coil size will in this case instead scale on the order of $N^{1/2}$. Solvents that meet these conditions are usually referred to as "theta solvents" in the lit-

erature. If $\chi > 1$, the description above breaks down (imaginary coil radius!), which can be interpreted as the excluded volume being overpowered from unfavourable solvent interactions, leading to the polymer forming globules and phase separate from solution (see Figure 2.1). Assuming a globule then takes up a volume of $V = Na^3$, this should then give polymer sizes scaling on the order of $aN^{1/3}$, since the size of the globule cannot be much larger than the volume occupied by the physical size of all monomers.

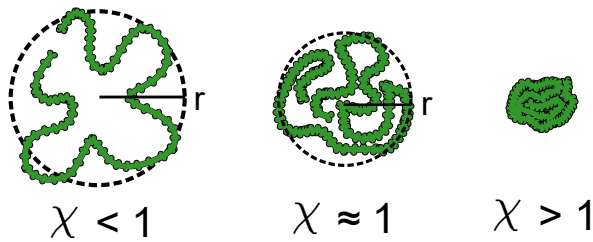

Figure 2.1: Polymer coils in a good, theta and bad solvent depicted from left to right.

2.2 Surface grafted polymers and polymer brushes

When one end of a polymer is attached to a surface and the rest of its chain remain free in solution, we can expect its coil to adopt a hemispherical "mushroom" shape bounded by the surface[18] (Figure 2.2a), where the polymer height h from the surface is roughly the same as its coil size r when free in the solvent. However, if the number of chains per area unit Γ (also known as the grafting density) of the chains is sufficiently high, the polymers can be forced to stretch out into a "polymer brush" configuration (h > r) in order to avoid overlapping their coils[19]. In Figure 2.2b the polymer brush case is depicted in comparison with the mushroom case using the average grafting distance $D = \Gamma^{-1/2}$.

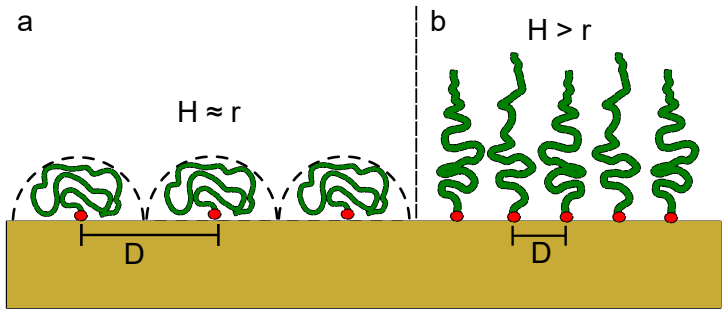

Figure 2.2: Polymers grafted to a surface adopting: **a** the mushroom configuration, or **b** the brush configuration.

To theoretically describe a polymer brush layer, we can adopt the same way of thinking as in the Flory theory, but replace the coil size r with the coil height h. Each polymer chain will then occupy a volume of h/Γ instead of r^3 as was the case in equation 2.1. The free energy as a function of height can then be written as:[13], [17], [19]

$$G(H) = \frac{3k_BTh^2}{2abN} + \frac{k_BTv\Gamma N^2}{h}\left[1-\chi\right] + C \tag{2.5}$$

If we then assume a very good solvent where $\chi = 0$ for simplicity, and solve for h by taking the derivative $= 0$, we arrive at the polymer brush height:

$$H = \left[\frac{abv\Gamma}{3}\right]^{1/3} N \tag{2.6}$$

We can then see how the polymer brush height H scales linearly with the degree of polymerisation and depends weakly on the grafting density. However, this description is only valid for strongly stretched brushes, because it assumes that the free end of the polymer chain is always located at H. Furthermore, the model assumes a constant monomer concentration within the brush volume, but it can be shown that the monomer concentration is more likely to adopt a parabolic density profile with respect to distance from the

surface[19], [20] as depicted in Figure 2.3.

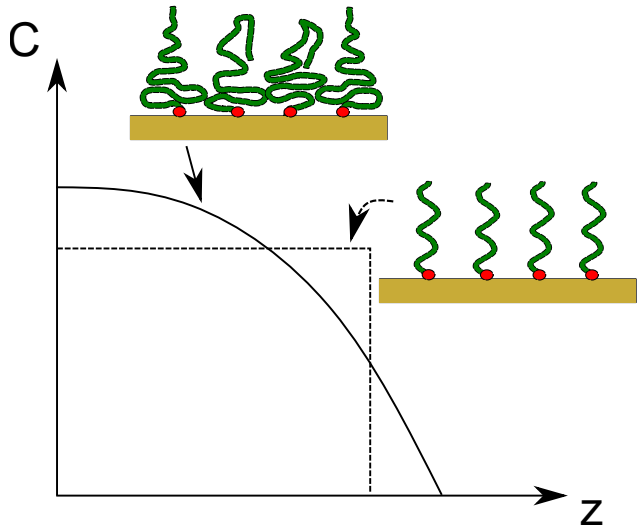

Figure 2.3: The monomer concentration C as a function of distance z from the surface. The dashed line represents the assumption of a strongly stretched brush (Alexander - de Gennes brush) while the solid line instead represents a parabolic monomer distribution.

2.2.1 Grafting strategies

In order to graft polymers with one end attached to the surface, the end-terminus of the polymer need a functional group that can bind directly to the surface atoms or to a corresponding functional group that has been previously attached to the surface. There are two approaches to this, either we attach already existing polymer chains with a functional group to the surface by adsorption, known as "grafting-to", or we functionalise the surface with an initiator group from which we can grow the polymer in a polymerisation reaction, known as "grafting-from". Both approaches have their advantages and disadvantages. Because of the small space taken up by the initiator molecule, grafting-from can achieve higher grafting densities and polymer brush heights compared to grafting-to in the same solvent conditions, where the grafting

density and brush height is limited to how closely the adsorbing polymer coils can pack on the surface. Additionally, since the grafting-from chains are grown continuously over time, it is possible to control the height of a formed polymer brush layer by selecting a certain polymerisation time. On the other hand, accurate quantification of the grafting density becomes difficult in the grafting-from approach, since there is currently no good way of quantifying the degree of polymerisation or average molecular weight of polymer chains grafted to a surface[21]. All in all, the selection of grafting method is an important consideration, but can sometimes also simply come down to which method works at all for the polymer of interest.

In this work, a grafting-to cloud point approach[13] was used to form highly stretched PEG polymer brushes from a thiolated PEG with average molecular weight of 20 kDa. The method relies on grafting the PEG dissolved at the solubility limit of a very kosmotropic salt (0.9 M Na_2SO_4), which competes with the PEG for surrounding water interactions, effectively turning the solution into a theta solvent for PEG and minimizes the polymer coil size without phase separating. The thiol end-group on the PEG is able to form bonds with gold surfaces, where they may also laterally diffuse and rearrange after initial formation[22]. The strength of the bond is higher if the gold surface has been oxidized[23], which is readily achieved if exposed to oxygen radicals during e.g. pirahna cleaning[23] or UV/O_3 treatment[24]. Once the PEG has bound to the gold surface, the solvent can be switched to regular water or a suitable buffer solution, which will cause the attached chains to stretch away from the surface and form a polymer brush as to lower their free energy in the new PEG-favourable solvent conditions.

2.3 Poly(ethylene glycol)

Poly(ethylene glycol) (PEG) is a linear hydrophilic neutral polymer with the chemical formula $C_{2n}H_{4n+2}O_{n+1}$ and a molecular structure pictured in Figure 2.4a. The most notable applications for PEG is within biomedicine and biotechnology, where due to its non-toxicity and increased circulatory lifetime of PEG-covered proteins and nanoparticles has become an integral part in various drug delivery systems[11], [25]. The increased circulation time of

PEG-covered particles comes in large part from the PEG chains ability to resist non-specific protein interactions, thus delaying targeting mechanisms of the immune system. Previous studies have also shown that PEG displays excellent protein-repelling properties when grafted densely to surfaces in the form of a polymer brush[13] and may even block entry of proteins in nanosized apertures despite consisting mostly of water[12].

While the full mechanism behind the protein repelling ability of PEG is still debated, the common properties of PEG and other polymers with similar properties are high hydrophilicity, presence of hydrogen bond acceptors but not donors and flexibility[25]. The classical explanation for the high hydrophilicity of PEG relates to the gauche configuration of the PEG-backbone (Figure 2.4b) and its favourable orientation for hydrogen bonding with water. However, a more recent study points toward the increased electronegativity of the oxygen atoms in the backbone playing a more important role in formation of strong hydrogen bonds[26].

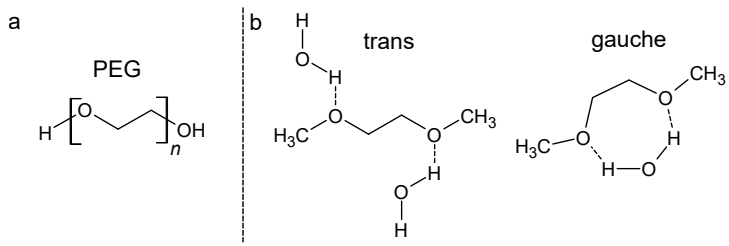

Figure 2.4: a Molecular structure of PEG. **b** Trans and gauche configurations of PEG backbone and their hydrogen bonding interaction with water molecules.

Since PEG is a relatively well studied polymer when it comes to its physical properties[27]–[30], decent estimates of its chain related physical parameters (section 2.1) can be made[12], where $a = 0.3$ nm, $b = 0.7$ nm and $v = 0.07$ nm^3 for water at room temperature (including χ) . For a 20 kDa PEG with $N = 456$ such as was used in **Paper 1**, this results in an estimated coil size of 17 nm.

2.4 Poly(methacrylic acid)

Poly(methacrylic acid)(PMAA) is a linear polyacid with the chemical formula $C_{4n}H_{6n}O_{2n}$ and structure as depicted in Figure 2.5. Polyacids are polymers that carry acidic groups along their polymeric backbone, which in PMAA's case is a carboxylic acid group located on every monomer. The carboxylic acid group further classifies PMAA as a weak polyelectrolyte, because the acid dissociation of the carboxylic acid group into a carboxylate group -COO(-) is reversible with a dependence on solution pH. However, ionizing monomer groups along the polymer chain leads to additional free energy costs compared to the monomer by itself due to the electrostatic repulsion between neighbouring charges[31]. This means the acid dissociation constant K_a of PMAA will be slightly lower compared to the K_a of the free monomer at the same conditions.

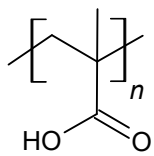

Figure 2.5: Molecular structure of PMAA.

The acid dissociation constant of a polyacid in solution is given by the relation[32]:

$$pK_a = pH + log_{10}\left(\frac{1-\alpha}{\alpha}\right) = pK_0 + A\alpha^{1/3} \tag{2.7}$$

where α is the degree of ionization, K_0 is the intrinsic dissociation constant at the limit of $\alpha \to 0$ (the first monomer unit to dissociate) and A is a constant depending on temperature, ionic strength and PMAA concentration. The pK_a and α at given conditions and PMAA concentration can be found from titration curves using a strong acid or base. pK_0 and A can be then be found

from the linear regression of pK_a and $\alpha^{1/3}$ [33]. For PMAA, equation 2.7 seems to be valid up to $\alpha \approx 0.2$ which corresponds to an estimated upper pH limit of 5.3 at close to physiological conditions with $pK_0 = 4.28$ and $A \approx 2.64$[32]. Thus, it is also possible to calculate e.g. the number of protonated monomer groups n_H of PMAA at a pH below 5.2, where n_H can be solved numerically from the adapted version of equation 2.7:

$$pH = 4.28 + log_{10}\left(\frac{N}{n_H} - 1\right) + 2.64\left(1 - \frac{n_H}{N}\right)^{1/3} \tag{2.8}$$

where N is the degree of polymerisation. Figure 2.6 gives the numerical solution to n_H in equation 2.8 for PMAA at physiological salt conditions (and slightly above and below).

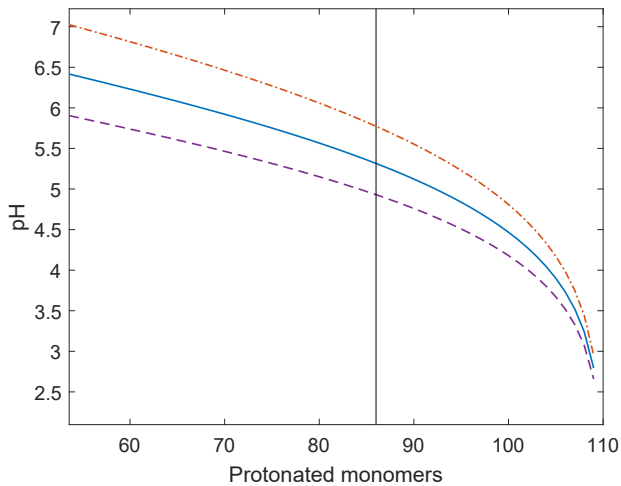

Figure 2.6: Number of protonated monomer groups n_H as a function of solution pH for PMAA with $N = 110$. The blue solid line corresponds to physiological salt conditions ($A = 2.64$), while the violet dashed line corresponds to above physiological salt concentration ($A = 2.0$) and the orange dash-dotted line to below physiological salt concentration ($A = 3.4$). The model can be considered valid for the number of monomer groups above that indicated by the black vertical line.

A charged polyelectrolyte tends to have a significantly swelled polymer coil in solution compared to the corresponding uncharged polymer chain (such as a weak polyelectrolyte at low pH where $\alpha \to 0$). This is due to two effects[34]. An increasing number of repulsive charges along the polyelectrolyte chain will cause intra-polymer repulsion and effectively lead to an increase in the chain stiffness b. As we can see from equation 2.1 this decreases the chains conformational entropy and thus to counter the new free energy, the polymer will increase its coil size until it balances out. In addition to this, coulombic charges will attract polar molecules such as water, meaning that the polymer-solvent interactions in aqueous solutions will increase and cause an additional swelling to lower the excluded volume term in equation 2.1. Since the presence of counter-ions in solution will effectively screen the charges and their intra-polymer repulsion along the polyelectrolyte chain, an increase in ionic strength of the solution will shrink the size of a polyelectrolyte coil.

2.5 Hydrogen-bonded interpolymer complexation

For mixtures of polymers with monomer units containing suitable hydrogen bonding donor and acceptor groups, interpolymer complexes have been observed to form in solution as a function of solution pH[14], [33], [35]–[39]. The phenomenon seems to occur between weak polyelectrolytes containing carboxylic acid groups and with non-ionic polymers containing hydrogen bond acceptor groups (such as alcohols, ethers, acrylics, lactamates, sachharides etc.)[14].

Notably, the formation of the complexes only start below a certain critical pH_{crit}, above which no interaction occurs and the polymer mixtures are able to co-exist freely in solution. The formation is also completely reversible if solution pH is changed back to above pH_{crit} after complexes have already been formed. Several factors have been found to influence the acquired pH_{crit} for a given pair of complexing polymers, both originating from environmental conditions such as temperature and salt concentration, but also from properties of the polymers themselves such as polymer concentration and polymer molecular weight. Studies of interpolymer complexes formed between PEG and PMAA or PEG and poly(acrylic acid) (PAA) have also revealed that

hydrophobic interactions can further stabilise the complex, since the PEG-PMAA interactions become even stronger at increased temperature when hydrogen bonding usually decrease in strength, while the same effect is much less pronounced for PEG-PAA interactions[37] Aside from studies of interpolymer complexes in solution, the interpolymer complexation concept have also been studied as a system of constructing bottom-up layer-by-layer films [14], [40].

The properties of the PEG-PMAA interpolymer complex is of particular interest for the work presented in **Paper 1**. It has been found to form at a 1:1 monomer ratio and start forming around $\alpha < 0.1$-0.12 for PMAA[39], [41], which corresponds to a pH_{crit} of about 4.5-4.8 at physiological conditions according to the model in Figure 2.6. Small angle neutron scattering measurements of the chain interactions of PEG-PMAA complexes at low pH found that the chains "zip together" and that the complex display an increased density compared to either of the chains free in solution[41].

CHAPTER 3

Characterisation techniques

To fully grasp the complex interaction of PMAA and a PEG brush at low pH, several characterisation techniques had to be employed. This section aims to provide an adequate understanding of each technique necessary to understand the results from Paper 1.

3.1 Surface plasmon resonance

Surface plasmon resonance (SPR) is a sensitive optical (refractometric) label-free technique that can detect nanoscopic changes continuously, such as a few ng/cm^2 of molecules adsorbing in the immediate volume of a sensor surface. Most SPR instruments are set up with flow-cells with an inlet and outlet that not only allow measurements in dry conditions, but also liquids to be flowed across the sensor surface with controlled flow rates, which thus provide the SPR with real-time measurements capabilities. Additionally, depending on the instrument setup, some SPR instruments can simultaneously measure the refractive index of the bulk medium above the sensor surface, which provides additional information about the investigated system without the use of a second reference channel.

The SPR technique is based on a phenomenon which occurs in thin films of certain metals, such as gold or silver (or other materials with similar properties), that can form so called surface plasmons, a surface bound waveform of collective electron oscillations that form under certain conditions and propagates along the interface of the thin metal film and a dielectric (insulating) medium. Maxwell's equations for electromagnetic radiation can be used to derive a description of the propagation and the necessary conditions required for a surface plasmon. The result describes two wave vectors, one propagating in the x-direction along the surface boundary of the metal and one in the z-direction away from the surface boundary (see Figure 3.1). Since the z-component wave vector $k_{z,sp}$ can be described in terms of the x-component $k_{x,sp}$, we end up with the following dispersion relation[42], [43]:

$$k_{x,sp} = \left(\frac{\omega}{c}\right)^2 \sqrt{\frac{\epsilon_1 \epsilon_m}{\epsilon_1 + \epsilon_m}} \tag{3.1}$$

where λ is wavelength, $\epsilon_m = Re(\epsilon(\omega)) + iIm(\epsilon(\omega))$ is the frequency dependent complex dielectric constant of the metal film and ϵ_1 is the dielectric constant for the dielectric medium in contact with the metal surface. Within optics, the dielectric constant is related to the complex refractive index $\tilde{n}(\omega) = n(\omega) + i\kappa(\omega) = \sqrt{\epsilon(\omega)}$ of a given medium, where the refractive index $n = \mathrm{Re}(\tilde{n})$ describes the speed of light in the medium as a fraction of

light speed in vacuum and the extinction coefficient $\kappa = \mathrm{Im}(\tilde{n})$ describes the degree of absorption and scattering of light in the medium.

Since the surface plasmon also extends in the z-direction, it has an associated electric field E extending away from the surface plane into both surrounding media, as depicted in Figure 3.1. A common way to denote the extent of the electric field decay is to use the decay length $\delta(\lambda)$, which is defined as the distance from the surface where the field strength has decayed to 1/e. For the dielectric medium ϵ_1 the decay is given as:

$$\delta_1(\lambda) = \frac{\lambda_p}{2\pi}\sqrt{\frac{Re(\epsilon_m) + \epsilon_1}{\epsilon_1^2}} \tag{3.2}$$

where λ_p is the plasmon wavelength. In essence, the average dielectric constant within a distance of $\delta_1/2$ from the surface has a large impact on the specific $k_{x,sp}$ leading to surface plasmon formation[44].

In order for light to convert into surface plasmons, an impinging photon must be able to match the plasmon wave vector according to:

$$k_{x,ph} = \left(\frac{\omega}{c}\right)^2 \sqrt{\epsilon} = k_{x,sp} \tag{3.3}$$

Since the momentum of light from a beam travelling in air with $n = \epsilon = 1$ will always be insufficient in order to satisfy the plasmon condition described in equation 3.1, the missing momentum has to come from somewhere else. The most common ways to achieve this are by using a grating or attenuated total reflection (ATR) coupler, the principle behind the latter of which will be described here. In the Kretschmann-Raether configuration depicted in Figure 3.1, an incident monochromatic p-polarized light beam is directed through an optically denser medium, such as glass prism, that is in direct contact with a thin metal film connected to an opposing less optically dense dielectric medium ($\epsilon_1 < \epsilon_2$ in Figure 3.1).

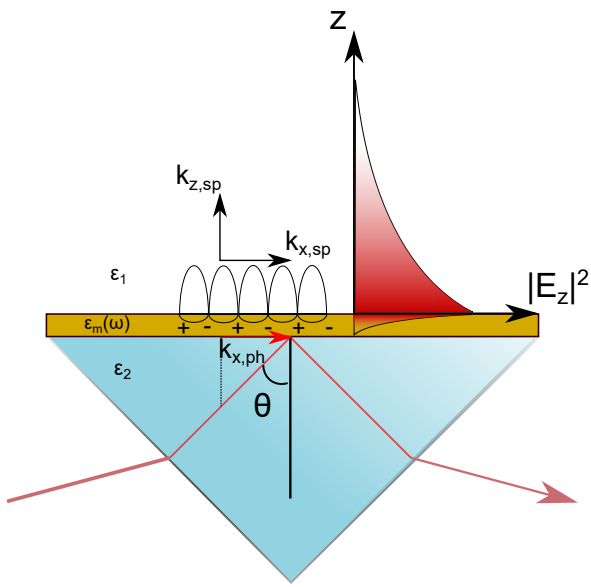

Figure 3.1: Surface plasmon excitation using the Kretschmann-Raether configuration.

As the light beam is reflected from the metal/prism interface above the critical angle of total internal reflection θ_{TIR}, a projected x-component of the incoming photon propagates with a wave vector $k_{x,ph}$ along the interface. The propagating wave component has an associated electric field extending perpendicular to the surface plane that is continuous also through the thin metal film into the dielectric on the other side, also known as an evanescent field. It is this evanescent field that allows the impinging photon to set up a surface plasmon at the metal/dielectric interface. At a certain incidence angle θ_{SPR}, the wave vector $k_{x,ph}$ is matched with $k_{x,sp}$, resulting in a sharp loss in reflected light intensity as a majority of the incoming light is absorbed by the metal through the evanescent field and transformed into surface plasmons, whose energy are eventually given off as heat. Figure 3.2 shows where the resonance angle θ_{SPR} and total internal reflection angle θ_{TIR} is found in an angular reflectivity spectrum obtained using the Kretschmann-Raether configuration.

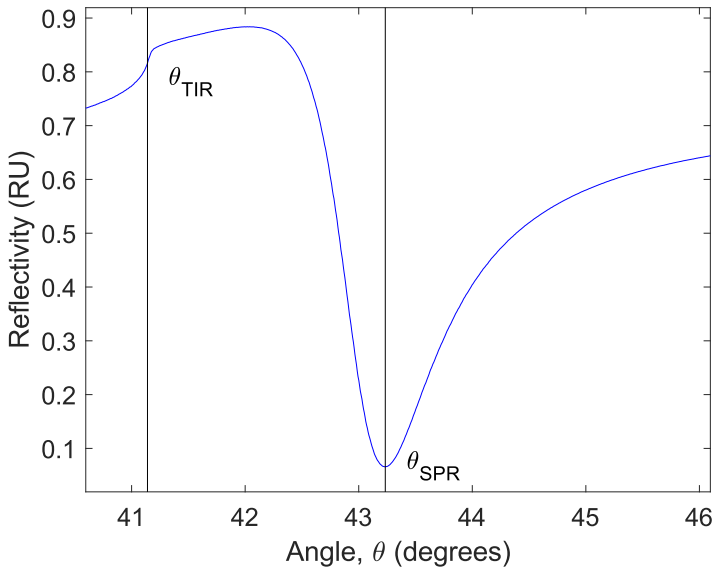

Figure 3.2: Surface plasmon resonance angular reflectivity spectrum for a $\lambda = 670$ nm light source reflecting in the Kretschmann-Raether configuration off of a 50 nm gold film exposed in air. Vertical lines are drawn at the θ_{TIR} and θ_{SPR} angles.

The high sensitivity of the SPR technique originates from the dielectric constant (and by extension refractive index) dependence of the surface plasmons, where even small differences in the average refractive index within the plasmon electric field above the metal surface will significantly alter the θ_{SPR} required for matching the plasmon wave vector $k_{x,sp}$. Selecting different wavelengths of the incoming light means different surface plasmon modes will be excited, where as implied from equation 3.2 longer wavelengths will sense further away from the surface compared to shorter wavelengths. Long wavelengths together with smaller angles enable studies of relatively thick films. However, due to the larger probing volume of longer wavelengths the sensitivity close to the surface will also decrease[45], meaning that the lowest possible wavelength is usually desired in practice.

3.1.1 Quantitative interpretation of the SPR response

Translating the angular response $\Delta\theta_{SPR}$ of a measured process in SPR requires an understanding of the properties of both the instrument and the investigated material. The relationship between the angular response $\Delta\theta_{SPR}$ and the corresponding change in refractive index units at the surface is[44]:

$$\Delta n_S = \frac{\Delta\theta_{SPR}}{S_{SPR}\left(1 - e^{\frac{2d}{\delta(\lambda)}}\right)} \tag{3.4}$$

where S_{SPR} is an instrument specific sensitivity constant, d is the thickness of the layer within which the change is occurring and $\delta(\lambda)$ is the decay length as given in equation 3.2. As can be seen, unless d is known or occurs within a large thickness where $d >> \delta$ (corresponding to a bulk change), it is difficult to calculate accurate refractive index changes of the surface layer without making assumptions about the layer thickness (which is feasable in some cases [44]). If the SPR instrument is able to measure $\Delta\theta_{TIR}$, this will have an additional sensitivity constant S_{TIR}, which is included in the relation of the bulk refractive index change given as:

$$\Delta n_b = \frac{\Delta\theta_{TIR}}{S_{TIR}} \tag{3.5}$$

For example, a MP-SPR Bionavis Naali 220A as the one used in **Paper 1** have $S_{SPR} = 121$ deg/RIU, $S_{TIR} = 77$ deg/RIU and a decay length roughly equal to $\delta(\lambda) = 218$ nm at a wavelength of 670 nm in water[13].

An important parameter for surface binding of a dissolved adsorbent, such as proteins or polymers, is the refractive index increment with concentration, $\partial n/\partial C$. It is possible to determine this from the $\Delta\theta_{TIR}$ of an SPR measurement by injecting a series of known concentrations of the adsorbant and perform a linear regression between the respective Δn_{bulk} and C, where $\partial n/\partial C$ is the slope of the fitted line. For PEG, $\partial n/\partial C = 0.1337$ RIU cm^3/g and for PMAA at pH 4.5 and physiological salt conditions $\partial n/\partial C = 0.1577$ RIU cm^3/g. The average generally accepted value for proteins is 0.182 RIU

cm^3/g[46].

The mass surface coverage m_S can be calculated (usually in ng/cm^2) from $\Delta\theta_{SPR}$ and estimates of d according to the general relation:

$$m_S = \frac{d\Delta\theta_{SPR}}{\frac{\partial n}{\partial C} S_{SPR} \left(1 - e^{\frac{2d}{\delta(\lambda)}}\right)} \tag{3.6}$$

However, at the limit of $d \to 0$ when $d << \delta$, it can be shown[13] that the surface coverage can be approximated as:

$$m_S = \frac{\delta\Delta\theta_{SPR}}{2\frac{\partial n}{\partial C} S_{SPR}} \tag{3.7}$$

3.1.2 Modelling of SPR measurements

Another way to extract the thickness and refractive index of an adlayer from SPR measurements without depending on estimates of the decay length δ (which is also influenced by the adlayer) is by theoretically describing the full angular reflectivity spectrum of an SPR measurement is using the Fresnel equations. The Fresnel equations describe how incoming light waves interact with different materials and originate from Maxwell's equations of electromagnetism, which means that they end up within a framework that also includes conditions for the formation of surface plasmons. In essence, the Fresnel equations provide Fresnel coefficients which describe how much light (in terms of the electric field vector E) is reflected, transmitted and absorbed as fractions (between 0 to 1) of incoming light as the light propagates between media of different refractive index. Due to the conservation of energy the coefficients must follow the relation[45]:

$$F_A = 1 - F_R - F_T \tag{3.8}$$

where F_A is describing the absorbed amount, F_R describes reflected amount and F_T describes the transmitted amount of light. For the application of sur-

face plasmons, we are interested in describing the p-polarised light component of the reflection and transmission Fresnel coefficients F_{Rp} and F_{Tp}. Consider e.g. the SPR case of a thin layer of thickness d, sandwiched between two semi-infinitely thick media as illustrated in Figure 3.3.

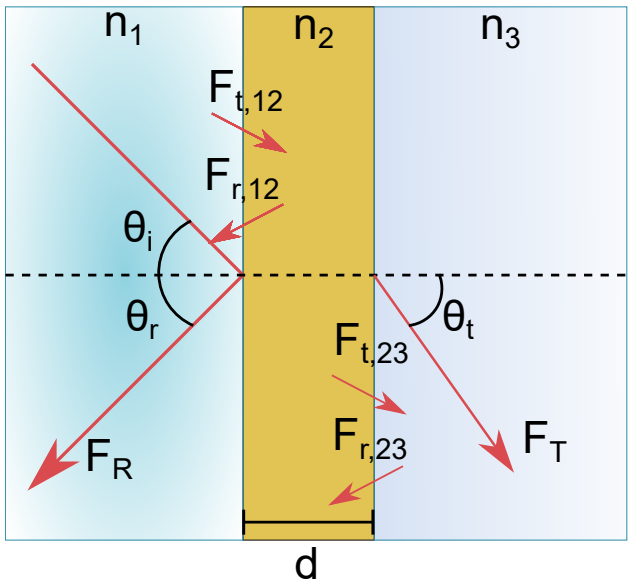

Figure 3.3: Light propagating through a thin film sandwiched between two semi-infinite media. The total amount of reflected and transmitted light across all three layers can be described by the amount of light reflected and transmitted at each interface.

For the case showed in Figure 3.3, the Fresnel coefficients F_{Rp} and F_{Tp} can be described according to:

$$F_{Rp} = \frac{F_{\mathrm{r},12} + F_{\mathrm{r},23} \mathrm{e}^{\mathrm{i}2k_0 d n_2 \cos(\theta_2)}}{1 + F_{\mathrm{r},12} F_{\mathrm{r},23} \mathrm{e}^{\mathrm{i}2k_0 d n_2 \cos(\theta_2)}} \tag{3.9}$$

and

$$F_{Tp} = \frac{F_{\mathrm{t},12} F_{\mathrm{t},23} \mathrm{e}^{\mathrm{i}k_0 d n_2 \cos(\theta_2)}}{1 + F_{\mathrm{r},12} F_{\mathrm{r},23} \mathrm{e}^{\mathrm{i}2k_0 d n_2 \cos(\theta_2)}} \tag{3.10}$$

For more complicated multi-layered systems, the transfer-matrix-method[45] can be employed for any number of intermediate layers j and medium m:

$$\Phi = \prod_{j=2}^{m-1} \left(\frac{1}{F_{\mathrm{t}[j-1]j}} \begin{bmatrix} 1 & F_{\mathrm{r}[j-1]j} \\ F_{\mathrm{r}[j-1]j} & 1 \end{bmatrix} \times \begin{bmatrix} \mathrm{e}^{-\mathrm{i}k_0 d_j n_j \cos(\theta_j)} & 0 \\ 0 & \mathrm{e}^{\mathrm{i}k_0 d_j n_j \cos(\theta_j)} \end{bmatrix} \right) \times \frac{1}{F_{\mathrm{t},[m-1]m}} \begin{bmatrix} 1 & F_{\mathrm{r},[m-1]m} \\ F_{\mathrm{r},[m-1]m} & 1 \end{bmatrix} \tag{3.11}$$

where the final coefficients for the reflection and transmission are found as:

$$F_{\mathrm{Rp}} = \frac{\Phi(2,1)}{\Phi(1,1)}, F_{\mathrm{Tp}} = \frac{1}{\Phi(1,1)} \tag{3.12}$$

In summary, if both the refractive indices and thicknesses of all layers are known but for one, the final unknown parameter can be determined from Fresnel model fits of the angular reflectivity spectrum around the θ_{SPR} sensitive region. However, as long as background matching (e.g. fitting measurements of an empty sensor) is performed on a sample prior to applying an adlayer of interest, the resulting parameters of all other layers do not need to be physically accurate. The reason why either the refractive index or the thickness of an adlayer needs to be known to determine the other is because of their convolution, i.e. they contribute to the SPR response in the same way. In the case of dry protein or polymer layers in air, the refractive index of their bulk counterparts can be considered a good approximation, which means their thickness can be determined very accurately so long as the layer can be considered homogeneous in three dimensions. If the density ρ and molecular weight M of the protein or polymer is known, the surface grafting density Γ can be determined according to:

$$\Gamma = \frac{\rho d N_A}{M} \tag{3.13}$$

where N_A is Avogadros constant.

Fresnel modelling can work also in liquid media. Since the effective refractive index of the bulk medium n_b can vary significantly with the presence and concentration of particulates or macromolecules, it will often become necessary to precisely determine n_b for every measurement in order to get an accurate model in liquid media. Snell's law of refraction, $n_1 sin(\theta_i) = n_2 sin(\theta_t)$, can be used to this end. It describes at what angle light is transmitted from one medium to another as it crosses the boundary between the two. However, when incoming light propagating from a medium of higher refractive index to that of lower refractive index above a critical incidence angle θ_c, there is no solution to the transmission angle θ_t where light continues through the medium of lower refractive index and light is instead reflected from the surface at an angle according to the law of reflection $\theta_r = \theta_i$. The critical angle denotes the start of the total internal reflection condition and this is the same θ_{TIR} that is measured in SPR. Thus, the average refractive index of the bulk medium $n_b < n_p$ can be calculated from an angular reflectivity spectra containing the θ_{TIR} according to:

$$n_b = n_p \sin(\theta_{TIR}) \tag{3.14}$$

However, for many types of adlayers the modelling results in liquid can become physically inaccurate, as solvent interactions can contribute to swelling and vertical heterogeneity, resulting in an effective refractive index that is a function of distance from the surface (such as the parabolic density profile of polymer brushes discussed in section 2.2) and often very hard to predict. Thus leading back to the problem of convolution of n and d.

3.1.3 Non-interactive probe method

When we do not know either the refractive index or the thickness of the investigated adlayer, direct Fresnel modelling run into accuracy problems as discussed in section 3.1.2. A solution to this problem termed as the "Non-interactive probe method" has been presented in the work of Schoch *et al.* 2013[47], where the height of protein repelling PEG brushes on an SPR sensor could be determined from "physically probing" the brush with proteins that

were repelled by the brush layer. The authors use a formalism where the vertical difference in sensitivity in the form of the decay length (equation 3.2) can be deduced using a reference PEG layer of lower molecular weight and a known thickness. However, since the decay length is also a function of refractive index of the adlayer, this approach could only produce sufficiently accurate results for adlayers within a refractive index range of 1.35-1.4, based on the choice of reference layer by the authors. The general principle behind the non-interactive probe method is illustrated in Figure 3.4.

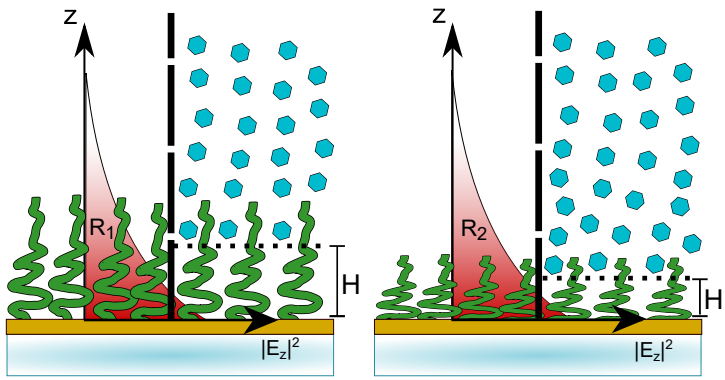

Figure 3.4: Illustration of the non-interactive probe method. The SPR response from a system containing, e.g. a polymer brush layer, with and without the presence of a probe (i.e. the brush layer must not be affected by the presence of the probe), can be used to extract an exclusion height above which the probe is repelled. This is possible due to the vertical difference in surface sensitivity originating from the decaying surface plasmon electric field. Thus, a shorter brush generates a larger SPR response compared to a taller brush during probe injection, since the probes are able to come closer to the surface ($R_2 > R_1$).

An improved version of the non-interactive probe method was presented by Emilsson and Schoch *et al.* 2017, where the decay length limitation could be avoided all together. The approach is based on performing separate Fresnel modelling for angular reflectivity spectra of the adlayer both with and without the presence of the probe molecule. The only difference between these two states will essentially be the n_{bulk} value. By applying the model to a range of plausible refractive indices for both states (with and without probe), a

corresponding range of possible exclusion heights can be extracted for both states. If the pairs of $[H, n]$ for both states are plotted together, the unique solution to the exclusion height and corresponding refractive index of the adlayer will present itself graphically as an intersect of the two curves (see Figure 3.5 c). This approach can be considered analogous to the algebraic problem of solving for two unknown variables using two sets of equations.

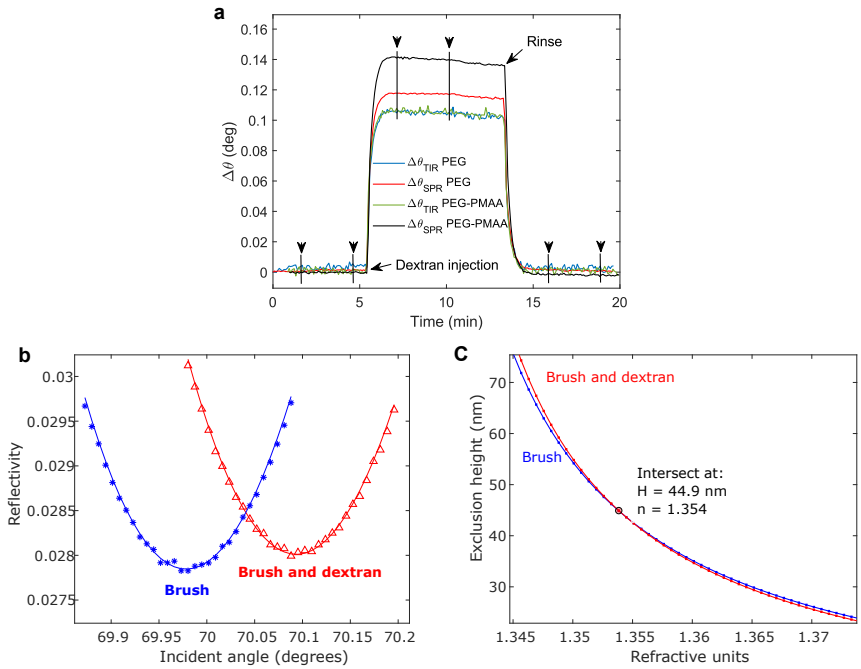

Figure 3.5: Examples of: **a** TIR and SPR signals during dextran injection on a PEG brush (blue and red respectively) and on a PEG-PMAA complex (green and black respectively). While the bulk refractive index is the same with and without adsorbed PMAA as shown in the two TIR signals, the SPR response is larger when PMAA is adsorbed. As the adlayer height shrinks from adsorbing PMAA, the probe molecules in the bulk liquid gets closer to the surface, leading to an increase in the SPR response. The arrows with accompanying vertical lines illustrate a typical range selection of the set of reflectivity scans used to acquire pairs of $[H, n]$ in the Fresnel modelling. **b** Fresnel model fits (solid lines) of averaged reflectivity spectra close to the resonance minimum for a PEG brush without probe (blue stars) and a PEG brush during dextran injection (red triangles). Given a range N of refractive indices n_N, the Fresnel model predicts an equal number of possible heights H_N. In **c** the pairs of $[H, n]$ are plotted for the brush with and without the dextran probe, resulting in an intersection where a unique solution to the brush H and n is found.

In the work presented in **Paper 1**, additional measures were taken to improve the quality of the exclusion height analysis. As exemplified in Figure 3.5a, sets of measurement points before, during and after probe injection was selected and turned into averaged angular reflectivity spectra (Figure 3.5b), which reduces the influence from measurement noise and reveals potential small scale interactions of the probe with the adlayer by comparing the two obtained exclusion heights per probe injection. Note that the exclusion height likely only describe the full extension of an adlayer if it is dense enough, as a probe may as well penetrate a certain distance into an initial low density region before it is repelled, e.g. a brush with a more pronounced parabolic density profile (see section 2.2). Similarly, the refractive index measured using the non-interactive probe method describes the adlayer as an optical field averaged density between the surface and the obtained exclusion height.

3.2 Quartz crystal microbalance with dissipation monitoring

Quartz crystal microbalance (QCM) is an acoustic characterisation technique for studying mechanical properties of thin surface layers in gaseous as well as liquid environments. Similarly to the SPR, QCM instruments are commonly set up to handle liquid flow across the sensor surface, which thus give them the same real-time measurement capabilities. The working principle behind QCM is based on the use of a piezoelectric quartz crystal that is cut along a specific crystallographic plane (AT cut), making it shear when exposed to an electric field (see Figure 3.6a). Applying an AC-voltage will cause shear oscillations in the QCM crystal and if the driving frequency matches the crystal's characteristic resonance frequency a standing wave will form through the crystal and the amplitude of the shear oscillations will be at a maximum.

The resonance frequency of the QCM crystal (and any of its odd numbered harmonics or "overtones") is intricately tied to its mechanical properties and the properties of the medium it oscillates in, meaning that if any of these properties change, such as its mass, the resonance frequency will also change[48] (see Figure 3.6b). This property can be utilised to create a microbalance capable of measuring changes in mass of deposited thin films or particles continuously, provided that the change can be viewed as an extension of the mass of the crystal itself. In order for that assumption to remain true, the added mass must be rigidly attached to the surface of the sensor, equally distributed in three dimensions and much smaller than the total mass of the crystal[49]. Following these criteria, the Sauerbrey equation[50] provides a linear relationship between the change in areal mass Δm and the response in resonance frequency shift Δf_n according to:

$$\Delta m = \frac{-C\Delta f_n}{n} \tag{3.15}$$

where C is a sensitivity constant dependant on the intrinsic properties of the QCM crystal (17.7 ng/cm^2 for AT-cut f_0 = 5 MHz) and n = 1, 3, 5, 7... is the overtone number. Note that Δm is a total mass change, meaning that

the mass of any solvation layer coupled to the particles is also included in the frequency response. If the formed layer's density ρ is known, the areal mass determined from the Sauerbrey equation can be used to derive the layer

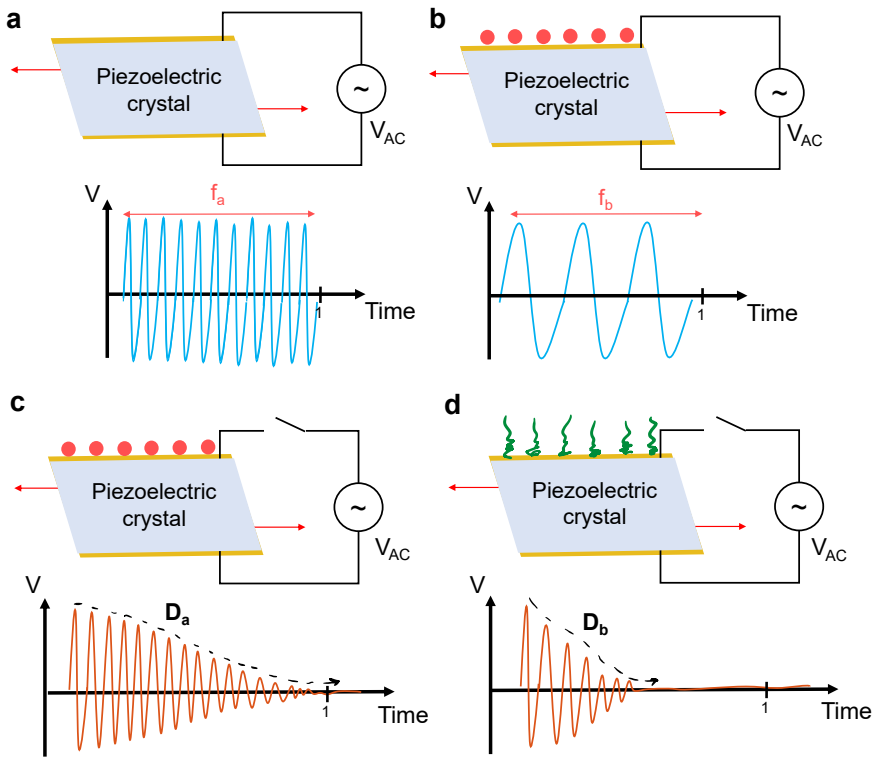

Figure 3.6: Basic principles of QCM-D. **a** Clean QCM-D crystal oscillating in shear mode at its resonance frequency, f_a, when an AC-voltage is applied to the contacts on either side of the piezoelectric material. **b** The same QCM-D crystal with rigid particles adsorbed to the surface yields a lower resonance frequency $f_b < f_a$ due to the increased mass of the system. **c** When the AC-voltage is turned off, the oscillation eventually dies due to the energy dissipating to the surrounding with a given dissipation factor D_a. **d** If the adsorbed layer is viscoelastic or "soft", the energy dissipation will be higher due to higher losses in the system, resulting in a higher dissipation factor $D_b > D_a$ compared to a more rigidly adsorbed surface layer.

thickness. If the layer deposited on the QCM crystal is not rigidly attached to the surface and instead should be considered "soft", i.e. possessing significant viscoelastic properties, the resonance frequency response will be dampened by the additional energy dissipation caused by the viscous and elastic properties of the layer, meaning that a non-linear frequency dependency exists and the Sauerbrey equation no longer holds. For studying viscoelastic materials in liquid environments, Quartz crystal microbalance with dissipation monitoring (QCM-D) provides additional useful information by also measuring the dissipation factor D_n defined as:

$$D_n = \frac{1}{\pi f_n \tau} \tag{3.16}$$

where τ is the decay rate of the amplitude as the driving AC-voltage is turned off[49]. An increasing viscous or elastic behaviour will cause more energy dampening and thus show up as an increase in the dissipation signal (see Figure 3.6 c and d).

Measuring Δf and ΔD at several overtones can provide additional insights. While each overtone has the highest sensitivity in the center of the sensor[51], the sensitivity area decreases radially towards the center with increasing overtone number. For this reason, the fundamental frequency (n = 1) can occasionally be prone to noise originating from the electrode contacts along the edge of the sensor surface, in which case measurements at higher overtones are preferable. The viscous penetration depth δ (the vertical sensitivity) also slightly varies depending on frequency (stretching between 400 to 110 nm between 5 to 65 MHz), leading to differences in sensitivity between different overtones. Measuring at several overtones can also reveal if Δf and ΔD have a frequency dependence due to viscoelastic influences by looking for increasing or decreasing overtone separation as changes occur in the adlayer[52][53]. A practical rule of thumb for asserting whether a deposited film can be considered rigid or viscoelastic is to also consider the ratio of change in Δf and ΔD, where an adlayer can be considered rigid if $\Delta D_n / -(\Delta f_n / n) \ll$ 4e-7 Hz^{-1}[48].

3.2.1 Kelvin-Voigt viscoelastic modeling

To better understand the mechanical properties of a viscoelastic layer, another model than the Sauerbrey equation must be used. One model described by Voinova *et al.*[54] is based on a mechanics approach where the viscoealstic layer is viewed as a continuous mass undergoing shear deformation. By mathematically treating the viscoelastic layer as a Kelvin-Voigt element (see Figure 3.7a), i.e. following the behaviour of a dashpot and a spring connected in parallel, both the viscous and elastic components' contribution to the stress/strain response from a resulting shear deformation can be derived:

$$\sigma_{xy} = \mu \frac{\partial u_x(y,t)}{\partial y} + \eta \frac{\partial v_x(y,t)}{\partial y} \tag{3.17}$$

where σ_{xy} is the shear stress, μ is the elastic shear modulus, $\partial u_x(y,t)$ is the displacement in x-direction, η is the shear viscosity and $\partial v_x(y,t)$ is the displacement velocity. From the wave equation of bulk shear waves we can further describe the displacement that occurs on the QCM-crystal surface:

$$\frac{\partial^2 u_x(y,t)}{\partial y^2}(\mu + i\omega_d \eta) = -\rho \omega_d^2 u_x(y,t) \tag{3.18}$$

where ω_d is the angular frequency of the displacement.

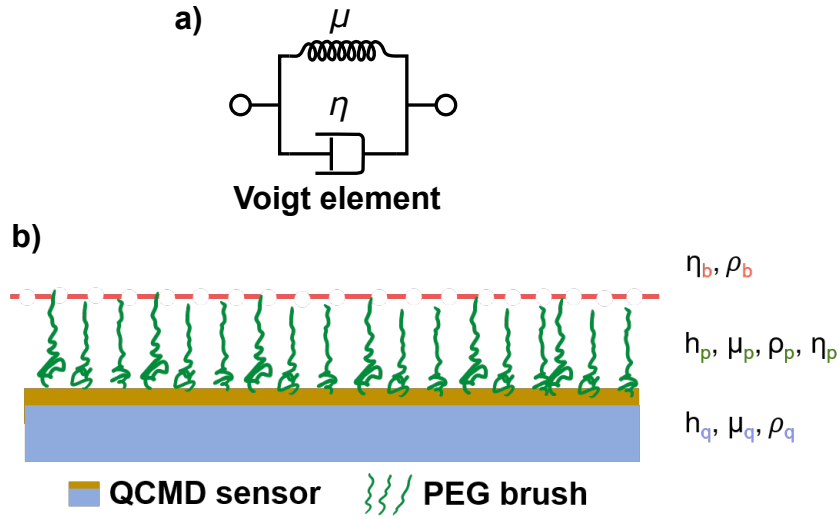

Figure 3.7: Schematic illustrations of **a)** Voigt viscoelastic element consisting of a spring and a dashpot connected in parallel and **b)** parameters considered in Kelvin-Voigt modelling representing the relevant mechanical properties of the QCM-D sensor (q), grafted PEG layer (p) and bulk solution (b).

Combining equation 3.17 and the general solution of $u_x(y,t)$ to equation 3.18 with no-slip boundary conditions[54], it is possible to describe Δf and ΔD in terms of the mechanical properties of the QCM-D crystal, the viscoelastic adlayer and the bulk medium. In Figure 3.7b the case with a viscoelastic PEG brush in liquid is illustrated along with each layer's relevant parameters and the corresponding relations for Δf and ΔD are given in equation 3.19 and 3.20 respectively.

$$\Delta f_n \approx -\frac{1}{2\pi\rho_q h_q}\left\{\frac{\eta_b}{\delta_b} + h_p\rho_p\omega_n - 2h_p\left(\frac{\eta_b}{\delta_b}\right)^2 \frac{\eta_p\omega_n^2}{\mu_p^2+\eta_p^2\omega_n^2}\right\} \tag{3.19}$$

$$\Delta D_n \approx \frac{1}{2\pi f_n\rho_q h_q}\left\{\frac{\eta_b}{\delta_b} + 2h_p\left(\frac{\eta_b}{\delta_b}\right)^2 \frac{\mu_p\omega_n}{\mu_p^2+\eta_p^2\omega_n^2}\right\} \tag{3.20}$$

where $\omega_n = 2\pi f_n$ and f_n is the prior frequency value and the viscous penetration depth δ is described as:

$$\delta_b = \sqrt{\frac{2\eta_b}{\rho_b \omega_n}} \tag{3.21}$$

Equation 3.19 essentially tells us how the interaction of three terms tied to the quartz crystal properties will affect its resonance frequency response to changes in any of the three layers. The first term corresponds to the liquid bulk properties and how far the acoustic wave penetrates into the bulk; the second term corresponds to the total mass loading from the adlayer; and the third term corresponds to the viscoelastic properties of the adlayer and its interactions with the bulk liquid. From the opposing sign of the viscoelastic term the dampening effect due to viscoelasticity also becomes apparent. From equation 3.20 we also see how the energy dissipation is disconnected from the mass of the adlayer, while liquid bulk contributions are still relevant alongside the viscoelastic properties.

In order to utilise equation 3.19 and 3.20 for fitting against measurements of Δf and ΔD, one would need to know all but two of the four adlayer parameters to determine the remaining unknowns. However, by using data from two or more overtone measurements when Δf and ΔD has a significant frequency dependence more than two unknown parameters can be determined. Still, because there is no unique solution to η_p or ρ_p[53], at least one of these parameters must always be given. Due to the assumptions of the Kelvin-Voigt approach, equations3.19 and 3.20 are applicable for polymer layers which are far from their glass transition regions, do not flow and try to retain their shape[54].

3.3 Surface force apparatus

A Surface force apparatus (SFA) is an instrument setup capable of simultaneously measuring the radial force and distance between two approaching cylindrical surfaces with high resolution. The vertical distance between the

two cylindrical surfaces can be measured using multiple-beam interferometry (MBI) down to sub-nanometer resolution, provided that the surfaces have been optimally prepared[55]. Multiple-beam interferometry in the SFA is based on the appearance of fringes of equal chromatic order (FECO) in a spectrogram when collimated white light is directed normally through the semi-transparent cylindrical surfaces. The wavelength separation between these fringes as well as their shape contain information on the distance between the two surfaces. At the same time, the radial force exerted between the surfaces can be measured by having one surface connected to a cantilevered spring and another to a piezoelectric element[56]. By comparing the calibrated expected displacement when a voltage is applied to the piezoelectric element to the actual displacement between the surfaces, any discrepancy can be taken as deflections in the spring, which may then be converted into a radial force if the spring constant is known. The force can also be measured independently of the optically determined distance if a semi-conductor strain gauge is connected to the spring and calibrated against known weights [57], [58]. Since both surfaces can be functionalised with different types of molecules before being installed, a SFA is excellent at probing many different types of surface phenomena and adlayer properties. The particular SFA setup used in the experiment described in **Paper 1** is illustrated in Figure 3.8.

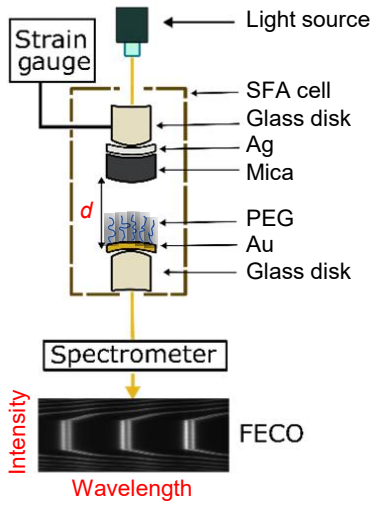

Figure 3.8: Schematic example of the SFA setup used for measuring the compression of a PEG brush in **Paper 1**.

To better understand the results from SFA measurements the radial force - distance curves need to be fitted by a suitable theoretical model. For polymer brushes repelled by a plain curved surface, the Alexander - de Gennes theory of stretched polymer brushes together with the Derjaguin approximation for forces acting between curved surfaces gives the following relation[59]:

$$\frac{F(D)}{R} = \frac{8k_BT\pi H}{35D^3}\left[7\left(\frac{H}{d}\right)^{5/4} + 5\left(\frac{d}{H}\right)^{7/4} - 12\right] \tag{3.22}$$

where D is the average grafting distance, H is the polymer brush height and d is the measured separation. This model is capable of describing the repulsion behaviour of a polymer brush with a constant density profile as it meets a surface. However, the model fails to explain measurements at further distances and predicts a quicker drop in repulsion than what is measured[59]. This may be attributed to a parabolic density brush as discussed in section 2.2.

CHAPTER 4

Interpolymer complexation of a PEG brush

The following chapter aims to provide an in-dept explanation of the central results from the PEG-PMAA surface interactions presented in **Paper 1** and guide the reader in how to interpret the surface characterisation data.

4.1 PMAA adsorption on gold

Before going into detail on the PEG-PMAA complexation, it is advantageous to understand what happens when only PMAA adsorbs to a plain gold surface and how the SPR and QCM-D measurements should be interpreted. Both SPR and QCM-D measurements of the adsorption process of PMAA on a clean gold surface and the effect of changing solution pH are given in Figures 4.1A and B. Starting with the SPR measurement in Figure 4.1A, as PMAA is injected into the flow-cell and exposed to the sensor surface at pH 4.5, we see an increase in the plasmon resonance angle shift $\Delta\theta_{SPR}$ from the initial baseline, indicating that PMAA adsorbs or interacts with the surface for these conditions. When the PMAA solution is rinsed out and changed back to the initial pH 4.5 solution, we can see that the signal decreases at first, but over time stabilises at a higher level than the initial baseline. This suggests that some PMAA polymer chains remain on the surface and are adsorbed irreversibly to the gold. Using $\Delta\theta_{SPR} = 0.1368$ deg and assuming equation 3.7 holds, an areal mass coverage of 78 ng/cm^2 is obtained for PMAA together with any associated counterions.

Raising the pH to 7.5 or even 11 seems to have a some effect on the amount of adsorbed PMAA as we can see the signal decreasing slightly over time, but after switching back to the initial pH 4.5 it is evident that some PMAA still remains on the surface. An experienced SPR user could also notice that the magnitude of the signal shifts between high and low pH is far greater compared to the equivalent bulk changes on an empty gold surface. In fact, since the SPR is only sensitive to effective refractive index changes, these signals likely correspond to pH dependent association and dissociation of counterions confined around the adsorbed PMAA chains similarly to what can be observed for PMAA brushes[60].

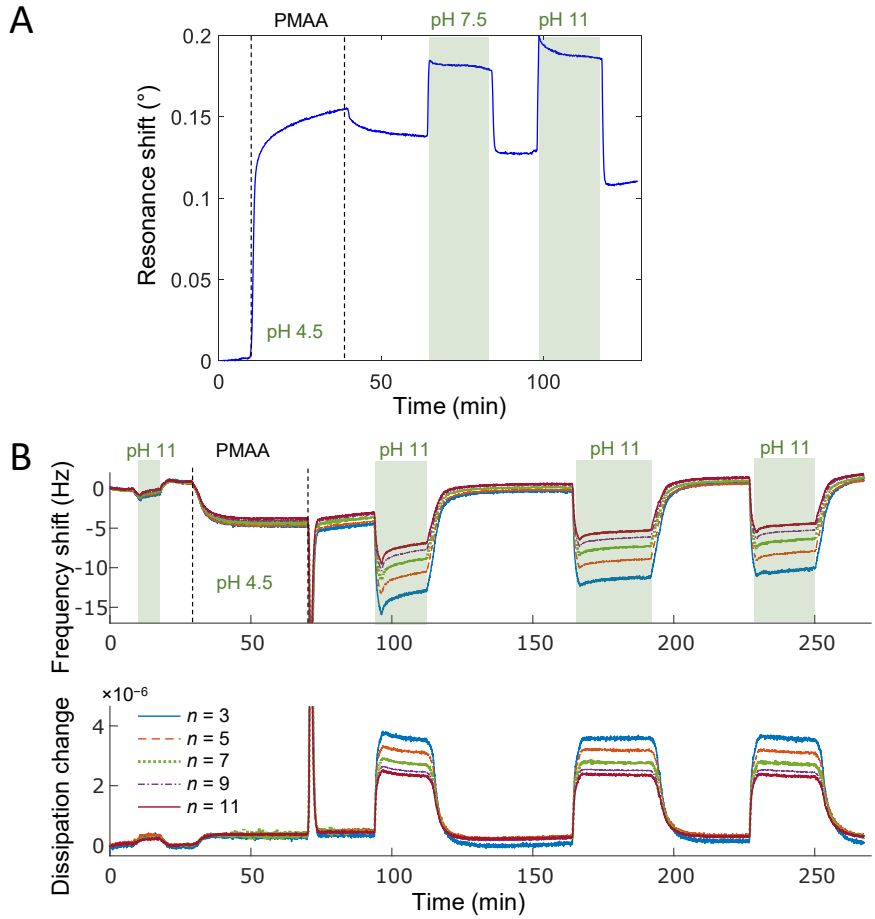

Figure 4.1: SPR measurement of PMAA adsorption (0.1 mg/ml) on a plain gold surface at pH 4.5 conditions (unless marked otherwise). **A** SPR measurements showing the real-time trace of $\Delta\theta_{SPR}$ at 670 nm of a PMAA injection and two following high pH injections. **B** QCM-D measurements showing the real-time trace of Δf compensated for overtone number (so actually $\Delta f/n$) and ΔD at several overtones for a PMAA pH 4.5 injection and repeated pH 11 injections.

Let us now take a look at the corresponding measurement in QCM-D (Fig-

ure 4.1B). The negative frequency shift $\Delta f/n$ (from now on only referred to simply as Δf) tells us similarly to SPR that PMAA is adsorbing at pH 4.5. Simultaneously, the dissipation signal ΔD does not shift significantly, meaning that PMAA adsorbs rigidly and is likely taking up a small volume on the surface, i.e. more of a "pancake" conformation compared to a "mushroom" as discussed in section 2.2. As PMAA is rinsed from solution at pH 4.5 (brief spike is from a bubble), the signals stabilise and we see that PMAA is irreversibly stuck to gold, agreeing with the SPR results. Checking the ratio of the -$\Delta D/\Delta f$ (section 3.2)gives $0.4e-6/5.7 = 7e-8 << 4e-7$ and so the Sauerbrey equation should be valid, giving an areal mass of 101 ng/cm^2 for the adsorbed PMAA together with coupled solvent and any associated ions. Comparing this to the same value given by SPR means around 23 ng/cm^2 of solvent molecules are coupled to the PMAA adsorbed to the surface.

When injecting a pH 11 solution, an increase in mass can be observed from Δf, which as we also concluded from SPR must be attributed to association of additional ions as PMAA becomes increasingly charged in addition to any potential increase of coupled water. Additionally, the increase in ΔD and splitting of the overtones suggests that the PMAA adlayer becomes viscoelastic, and we can conclude that the polymers change from a rigid flat conformation to a swelled conformation just like the case of a charged polyelectrolyte in solution (section 2.4).

As the high pH 11 solution is replaced with pH 4.5, both Δf and ΔD returns to their initial baselines giving the impression that the PMAA has been completely removed from the surface, thus completely contradicting the SPR measurement. However, considering that the magnitude of the signal is far too large during the switch from pH 11 to pH 4.5 compared to before PMAA is injected, PMAA must still be absorbed to the surface. The almost complete return to the baseline is remarkable, but could be explained by the PMAA once more adopting a more flat and even more stretched out conformation than when adsorbing from solution. A pH > 11 would make $\alpha = 1$ and could give PMAA more of a rod-like conformation in solution as observed for some strongly charged polyelectrolytes[34] and the following fast pH switch means the polymer chains will have very little time rearranging their conformation and could thus stick while still being significantly stretched out.

In conclusion, we now know that PMAA adsorbs to a gold surface irreversibly no matter the pH we use and we have seen that since the signals from a QCM-D measurement contain more information than e.g. a SPR measurement it also makes it more difficult to interpret and thus highlights the importance of using complementary characterisation techniques.

4.2 PMAA adsorption on a PEG brush

Since the pH_{crit} of the PEG-PMAA hydrogen bonding interaction in solution depends on several factors including environmental conditions, we used QCM-D to qualitatively investigate the actual pH_{crit} of the PEG brush and PMAA hydrogen bond interaction by sequentially injecting PMAA solution of decreasing pH until adsorption occurred. For PEG brushes with 20 kDa molecular weight and PMAA of molecular weights $\sim$ 8 kDa, 75 kDa and 483 kDa injected at a concentration of 0.1 mg/ml in physiological salt concentrations, a pH_{crit} of $\sim$ 5 was obtained. For the smallest molecular weight of PMAA at 1.3 kDa, the pH_{crit} is lower, ending up around pH 4. The amount of interacting polymer was found to be heavily dependent on pH below the pH_{crit} such that the signal from the adsorption of PMAA effectively doubled between pH 4.5 and pH 4.0. However, at a pH around 4 the PMAA started to visually self-precipitate (solution became cloudy) at the given salt concentration. Therefore, the pH of 4.5 was chosen as a good balance between adsorbed amount and minimizing risk of self-precipitation.

Introducing a PEG brush to the gold surface drastically changes the amount of PMAA binding to the surface at pH 4.5 as measured by SPR (Figure 4.2). Comparing the $\Delta\theta_{SPR}$ at 670 nm between Figures 4.1A and 4.2 we can observe an almost 10 fold increase in adsorbed mass. This, together with verifying from $\Delta\theta_{TIR}$ that the signal does not correspond to bulk liquid changes, suggest that the PMAA must interact with the PEG brush. As can be seen from the injection of PMAA at pH 7.5, the PMAA does not interact with the PEG brush at this pH and is also effectively blocked from interacting with the underlying surface, strengthening the role of hydrogen-bonding for these kinds of interactions. Upon repeated injections of a pH 7.5 solution a majority of the adsorbed PMAA desorbs from the surface. Considering that

the amount of PMAA binding to gold (Figure 4.1) is about 0.14 deg for the same injection length, at least part of the remaining amount should correspond to PMAA still bound inside the PEG brush. The amount left after PBS 7.5 injections varied between 0.15-0.3 degrees in repeated experiments however, even though the amount of adsorbed PMAA appeared the same.

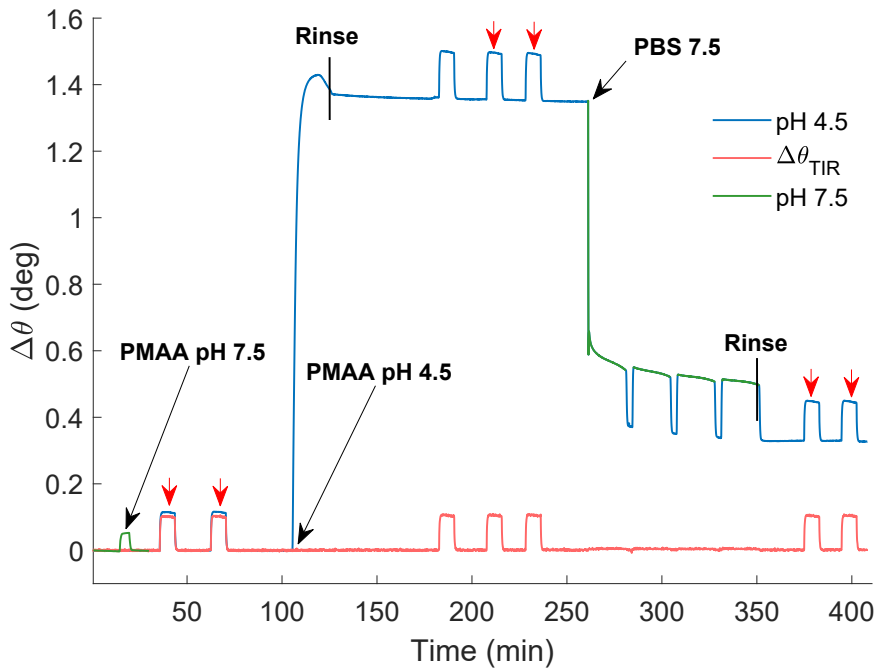

Figure 4.2: SPR measurements during injection of PMAA to saturation on top of a 20 kDa PEG brush at pH 4.5 and 7.5. The blue trail corresponds to $\Delta\theta_{SPR}$ at pH 4.5 and green trails to $\Delta\theta_{SPR}$ at pH 7.5. The red trail corresponds to bulk liquid changes via the $\Delta\theta_{TIR}$. Red arrows mark examples of selected height-probing injections with Dextran (10 mg/ml, 100 kDa, pH 4.5). Black arrows mark the starting points upon injecting PMAA (100 µg/ml, 8 kDa, pH 4.5) and PBS solution at 7.5. "Rinse" mark returning to pH 4.5 solution.

Similar "overshoot" phenomenon as the one occurring during the PMAA injection have been observed during polymer adsorption previously[61] and can

in this case be explained by how the PMAA chains initially binds in swollen conformations but have lower energy at low pH in a flat conformation (as discussed in sec 4.1) and thus will rearrange over time. This rearrangement is thought to be able to reduce the number of available binding sites on the surface and force excess adsorbed polymer chains to desorb.

Using Dextran as a non-interactive probe allowed for the determination of the exclusion heights H at three different stages of the experiment, as exemplified in Figure 4.2. The result from six repeated experiments is presented in Figure 4.3A, where each repeat represent a separately grafted sensor with an overall range of obtained PEG brush grafting densities Γ between 0.25–0.3 nm^{-2} (or equivalently D between 1.9–2.1 nm), as determined from Fresnel modelling (section 3.1.2) of dry measurements prior to liquid injections. Even if the initial PEG brush height varies, after PMAA is adsorbed the molecular probe is able to penetrate about 10 nm further into the brush layer, suggesting at least partial collapse of the layer even though a significant amount of mass is added. Furthermore, a pH of 7.5 seems sufficient to rinse the majority of adsorbed PMAA and restore the initial exclusion height of the brush.

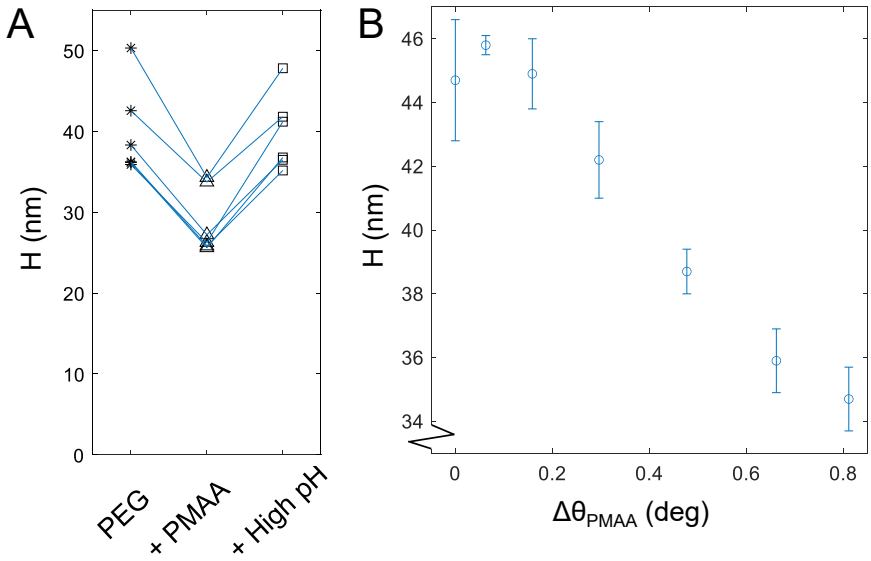

Figure 4.3: Averaged exclusion heights H determined using the non-interactive probe method for: **A** six repeated PMAA saturation experiments, and **B** six short PMAA injections on the same surface (error bars show the uncertainty of the analysis within 2 times the standard deviation).

To see how the exclusion height changes gradually with the amount of adsorbed PMAA, smaller steps of PMAA was injected with Dextran probing injections in between (Figure 4.3B). Here we see a clear downward trend in the exclusion height as more PMAA is added. In summary, the SPR measurements point towards the ability to tune the height of a PEG brush on a nanometer scale, which is an enticing concept for macromolecular gating of nanopores or nanochannels or actuating systems in nanostructures in general.

The ability of the PEG-PMAA interpolymer complex to retain the barrier property of a PEG brush at the required amount of adsorbed PMAA is investigated in Figure 4.4A. A model protein known as Avidin (which normally adsorbs to gold) is injected at pH 4.5 after a PEG brush is first saturated with PMAA and then once more after injecting several rounds of pH 7.5 solutions. When PMAA is present on the PEG brush, a large adsorption signal is detected from injecting Avidin. The signal after repeated pH 7.5 injections resembles that of remaining PMAA from previous experiments (Figure 4.2), suggesting that the protein adsorbs to the available PMAA chains that are not occupied by the PEG brush and then simply desorb when the PMAA desorbs at higher pH. After both PMAA and Avidin is rinsed in pH 7.5, an additional Avidin injection results in no adsorption and thus the barrier properties the PEG brush have been restored. From Figure 4.4B a plot of the protein response vs PMAA response gives an approximate limit around 0.2 degrees of adsorbed PMAA after which protein binding starts and the brush barrier properties start to become compromised.

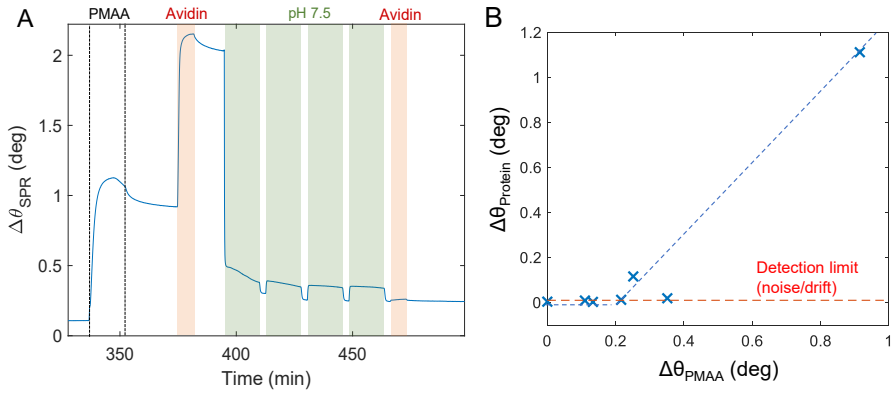

Figure 4.4: SPR measurements of a PEG brush where PMAA and Avidin is injected. **A** Avidin is injected first after saturating the PEG brush with PMAA and then a second time after repeated injections of pH 7.5 solutions. **B** Avidin signal plotted against the signal from short PMAA injections.

The adsorption profile measured with QCM-D (Figure 4.5A) for injection of PMAA on a PEG brush at pH 4.5 followed by rinsing in high pH is distinctly different to the same system measured using SPR. As PMAA is injected, Δf increases significantly for the lower harmonics, implying a net loss of mass on the surface. Only for the two lower frequencies a net gain in mass can be observed. Since acoustic mass account for coupled solvent and SPR shows a huge increase in dry mass this suggests that, as PMAA forms hydrogen bonds with PEG, a large amount of water is expulsed from the brush layer. Simultaneously, ΔD is significantly decreasing, suggesting that the adlayer goes from viscoelastic to more rigid. We find that when PMAA is adsorbed, the dissipation contribution of the polymer layer is $\Delta D \approx 3 \cdot 10^{-6}$. For comparison, this is lower than the change in dissipation caused by bovine serum albumin (a 66.5 kDa protein) on a plain gold surface[62]. In conclusion, the expulsion of water together with the significant increased rigidity speaks for compression of the PEG-PMAA layer, which is in agreement with SPR that demonstrated a negative change in exclusion height even though dry mass is added to the system.

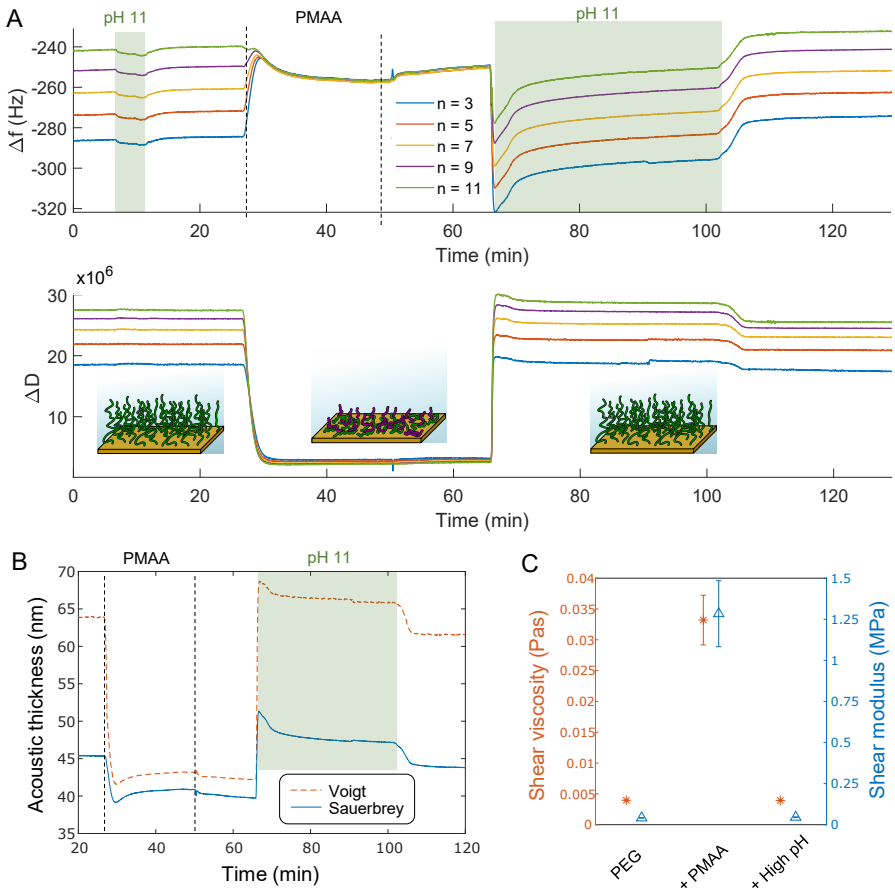

Figure 4.5: QCM-D measurement of a PEG brush at pH 4.5 as PMAA and a high pH solution is injected. **A** Δf and ΔD values relative to an empty QCM-D crystal for 5 different overtones. **B** Acoustic thickness h calculated using the Sauerbrey relation and Kelvin-Voigt modelling assuming a layer density of 1100 kg/m^3. **C** Shear viscosity η and shear modulus μ obtained from the Kelvin-Voigt model assuming a density of 1100 kg/m^3 Error bars show 2 times the standard deviation.

The Δf during injection of a higher pH solution suggests the system gains mass, which is contrary to the equivalent process observed in SPR. A similar

reasoning can be applied here, where the coupled water previously lost while PMAA was adsorbed now will go back into the PEG brush once the PMAA desorbs. In addition, ΔD increases to slightly above the initial baseline, since after restoring the PEG brush there is still an added fraction of PMAA remaining on the gold, which adopts a swelled conformation due to its increased charge density at higher pH. The ΔD and Δf change observed as the pH is switched from 11 to 4.5 indicates that the counterions dissociate as the PMAA becomes uncharged, similar to what can be observed for PMAA on gold in Figure 4.1B.

The values of Δf and ΔD in Figure 4.5A were used for modelling the change in acoustic thickness h throughout the PMAA adsorption experiment by fitting equations 3.19 and 3.20 to the experimental data. Since the viscoelasticity of the adlayer changes during the experiment, both the Kelvin-Voigt model applicable to viscoelastic films and the Sauerbrey relation applicable to rigid films were used and compared. A fixed density of 1100 kg/m^3 was selected as a good midway between the relatively similar densities of water, PEG and PMAA. Even if this might be an underestimation of the true density when PMAA is adsorbed to the PEG brush, using a density of for example 1200 kg/m^3 instead only shifted the resulting height by about 3 nm.

The change in h for the Kelvin-Voigt model compared to the exclusion height H from SPR is in clear qualitative and semi-quantitative agreement, where the adsorption of PMAA causes a significant change in height. Additionally, while the relatively small difference between h and H when PMAA is adsorbed can be explained from experimental or model errors, the discrepancy in initial and final PEG brush height between the viscoelastic Kelvin-Voigt model and the non-interactive probe method is significant. This is likely originating in the nature of how both techniques measures height and to the parabolic density profile of the PEG brush. The acoustic height obtained from the Kelvin-Voigt model can be thought of as the edge of the viscoelastic influence from the brush layer, which is perhaps not so easy to define. It could very well extend much further than the height at which the brush rejects physical probes, especially considering the full hydration layer of the brush. A similar trend between optical and viscoelastic thickness has been observed previously for other types of polymer layers [63]. Regardless, the QCM-D results agree with the SPR measurements with regards to the adaptable height of the polymer

layer.

However, the Sauerbrey relation gives excellent quantitative agreement between h and H at 1100 kg m^{-3} when PMAA is adsorbed and forms a rigid layer at pH 4.5 ($\Delta D/\Delta f$ = 1.2e-8 « 4e-7). From the Kelvin-Voigt model we could also extract the viscoelastic properties of the PEG brush throughout the experiment. Figure 4.5C shows how the viscosity goes from a value corresponding to 5 % 8 kDa PEG in water to something corresponding to 20-30 % 8 kDa PEG in water when PMAA is bound[64]. Furthermore, the elastic shear modulus reaches the order of magnitude of typical rubbers when PMAA is adsorbed, suggesting a behavior similar to cross-linking of polymers. Considering the rheological change, the compressed height and the water expulsion of the formed PEG-PMAA layer, it is questionable to refer to the layer as a polymer brush at this stage. At the same time, if the pH is raised above the pH_{crit} the PEG brush morphology and barrier properties seem completely restored.

As a final complimentary technique we turned to collaborators over at TU Wien in Austria who measured the compression of a similarly prepared PEG brush before and after adsorbing PMAA at pH 4.5 and then again at a pH of 7.5 when PMAA is desorbed. The resulting force-distance curves are presented in Figure 4.6.

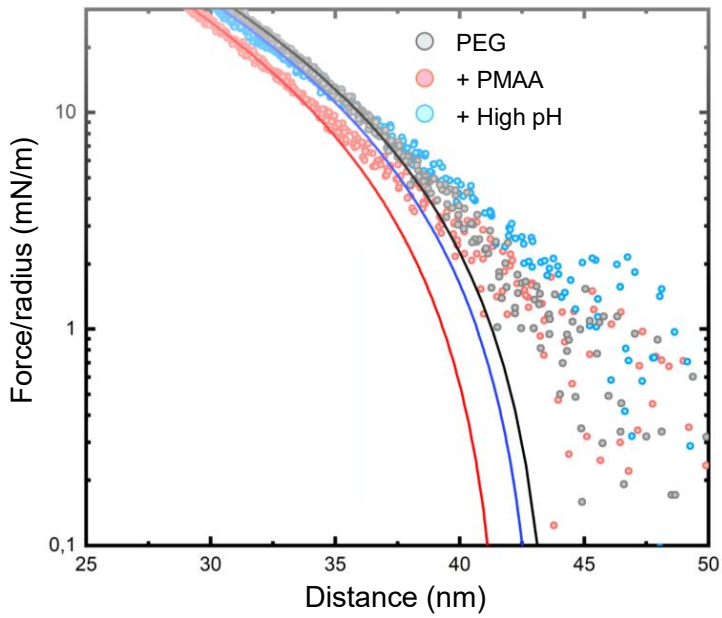

Figure 4.6: SFA measurement with the logarithmic radial force against linear distance from the surface. Included measurements are: PEG brush at pH 4.5 (grey dots), PEG-PMAA at pH 4.5 (red dots) and the same surface in a pH 7.5 solution (blue dots). The lines correspond to Alexander – de Gennes experimental fits (equation 3.22) for the respective measurement of matching colour.

As the probing mica surface approaches the PEG brush (large distances), only small repulsive forces can be detected around the noise limit of the instrument. As the mica approaches the brush it starts to become increasingly compressed and an increasingly large force is detected.

In the compressed regime $d < 35$–40 nm, the Alexander–de Gennes strongly stretched brush model fits rather well. However, at further separations the model underestimates the repulsive behaviour due to the constant polymer brush density assumption (section 2.2), which results in a smaller brush thickness compared to what could be observed in the measured data.

For the initial PEG brush in pH 4.5, both the average grafting distance D and the brush height H was allowed to vary. The resulting values of $D = 1.9$ nm and $H = 44$ nm both come within our expected value ranges as measured by SPR. Even though this will introduce an uncertainty for the initial PEG layer, if the acquired value for D is fixed for the other two measurements, the relative change in H should still be accurate. While the brush height as measured by SFA did not decrease as much as observed with SPR or QCM-D, the height obtained for SFA is in good agreement with the QCM-D measurements when PMAA is adsorbed.

CHAPTER 5

Nanopores

This chapter goes into details on the topic of nanopores, what they are, what they look like and how they can be useful in single-molecule experiments, as well as describe the particular plasmonic nanopore membrane of presented in **Paper 2**.

5.1 Solid-state and plasmonic nanopores

Solid-state nanopores have been receiving much attention for their potential in the field of single-molecule measurements, where they offer stability from environmental conditions and high design control of geometries not possible with biological nanopores, while still being able to resolve single-molecules using techniques such as ion current or force spectroscopy measurements in combination with the nanopores[7]. Furthermore, solid-state nanopores can be functionalised with a multitude of different coatings and molecules to increase their functionality and diversity needed for singe-molecules studies[8]. Another type of nanopore known as *plasmonic nanopores* have recently been utilized for single-molecule detection[65]. The sensing principle work either by direct refractometric changes in near-field confinements, or by enhancing the signal of techniques such as surface-enhanced Raman spectroscopy and fluorescence microscopy[66]. Plasmonic nanopores bring additional potential functionalities such as enabling electrochemistry, dielectrophoretic particle locomotion and resistive heating, all due to the conductive metal film and localised electric fields, which are otherwise lacking in plain solid-state nanopores[67].

Plasmonic nanopores may also be fabricated in large arrays where they acquire different properties. Short-range ordered nanopore arrays self-assembled from colloidal lithography or long-range ordered nanopore arrays patterned using techniques such as electron beam lithography (EBL) or ion beam lithography (IBL) can both produce nanopore arrays with plasmonic properties[67]. While isolated nanopores are necessary for studies of single-molecules in order to avoid ensemble averaging, nanohole arrays provide value for developing new types of functional nanopores. The larger scale of nanopore arrays allows for less demanding characterisation techniques while the critical geometrical nanopore properties are retained. This means that new functionalisation strategies (such as a macromolecular gating system) developed using nanopore arrays should also be readily applicable to individual nanopores. Figure 5.1 gives two examples of plasmonic nanopore arrays: "Nanowells", which are essentially nanoholes through a metal film extending some distance into a solid support[68], and "Nanopore membranes", i.e. nanoholes through a metal film and a support membrane, which are produced in **Paper 2**.

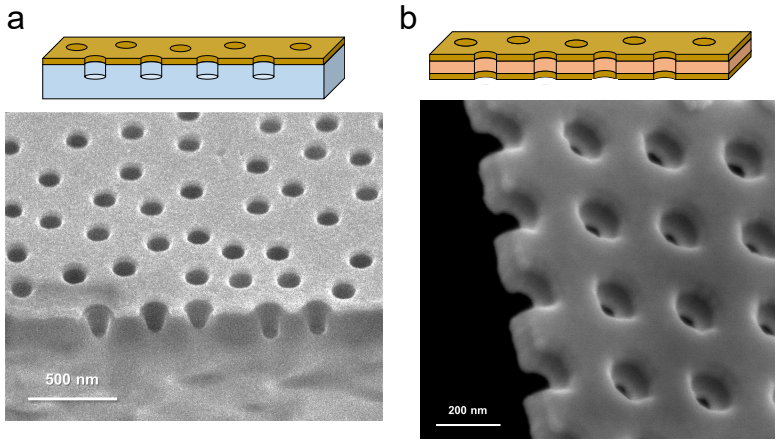

Figure 5.1: Illustrations and SEM cross-section images of two types of plasmonic nanostructures with gold metal films: **a** Nanowells and **b** Nanopore membranes as presented in **Paper 2**. This image contains adapted material under a Creative Commons license 4.0 (https://creativecommons.org/licenses/by/4.0/legalcode) from Malekian *et al.* 2017[68].

The refractometric sensing principle of plasmonic nanopores is the same as in the SPR technique discussed in section 3.1, but the plasmons are not excited with the same coupling mechanism. In plasmonic nanopore arrays, plasmons can be excited in two modes. The first is based on a grating coupling mechanism of which is more sensitive to refractive index changes around the gold-dielectric interface at the surface and originates from the increased momentum provided by Bloch Waves[69] (i.e. wave phenomenons arising from periodic structures). The second type of plasmon mode is providing increased sensitivity inside the pore cavity and behave similar to those of localised surface plasmon resonance occurring in conductive nanoparticles of various shapes and sizes[70], but can also be interpreted in terms of Fano interference between individual light transmitting pores and the grating coupled plasmons at the surface[71]. The refractometric sensing properties of plasmonic nanopore arrays together with complimentary fluorescence microscopy techniques, will be able to provide both label-free and labeled characterisation of macromolecular interactions in real-time. Thus, plasmonic nanopore arrays such as those

shown in Figure 5.1 provide an excellent way of testing if the interpolymer complexation system described in section 4 and **Paper 1** can be used for macromolecular gating of nanopores.

While the fabrication of long-range ordered nanopore membranes using EBL or IBL has been performed previously[67], the novelty of the specific structures prepared in **Paper 2** from a fabrication standpoint is that the walls inside the pores remain completely free of metal. This enables surface functionalisation of the metal while leaving the support material in the center of the pore free. It also makes the center walls of the pore susceptible to secondary functionalisations if desired, such as thin passivation layers or receptor molecules that allow for further functionality. Additionally, comparisons with short-range ordered nanopore membranes fabricated using colloidal lithography with similar parameters to the EBL nanopores showed similar optical properties in agreement with the Fano interference interpretation[71].

5.2 Fabrication of plasmonic nanopore membranes

As the main contribution to **Paper 2** include parts of the fabrication of the EBL nanopore membranes, this section provides a full description of the fabrication process including up-to-date improvements made after publication of **Paper 2**.

The nanopore membrane fabrication process starts with producing square SiN membranes as "windows" through a <100> Si 100 mm diameter substrate wafer, with the general processing steps as illustrated in Figure 5.2. The substrate wafer is first thoroughly cleaned by immersion into a 80°C solution of 5:1:1 v/v H_2O:NH_4OH:H_2O_2 (RCA1) for 10 minutes, followed by a 2 % HF solution for 1 minute and finally a 80°C 5:1:1 v/v H_2O:HCl:H_2O_2 (RCA2) for 10 minutes followed by rinsing in H_2O and spin drying. After the initial substrate cleaning, a 50 nm low-stress SiN layer was grown on both sides of the wafer using low pressure chemical vapour deposition (LPCVD) at 820° for 9 minutes.

Large squares of 800 x 800 μm are then patterned using conventional pho-

tolithography procedures. Here the first step is to spin coat a positive photoresist (Microposit S1813) layer on one of the SiN layers at 4000 RPM for 60 seconds, followed by baking the wafer on a hotplate at 120°C for 2 minutes to cure the photoresist layer. In the next step, the photoresist is exposed to UV-light for 10s through a patterned mask carrying the design pattern of interest and subsequently developed using a matching developer chemical (Microposit MF-319) for 1 minute and washing in H_2O immediately afterwards. After the development step, the underlying SiN layer should now be exposed in the patterned area only. This pattern is then transferred through the SiN layer to the underlying Si substrate with a Reactive ion etching (RIE) process using a mix of CF_4(g) and O_2(g) at 4:1 volume flow ratio, 50 W, 15 mTorr for 9 minutes to etch away the exposed SiN. Residual photoresist after RIE is removed using an O_2-plasma at 250 W, 500 mTorr for 2 minutes.

The wafer is then anisotropically etched at a 54° crystallographic angle using a strong 35 % KOH solution for 6-7 hours at 80°, until the bottom SiN layer is reached and windows approximately 120 x 120 μm^2 in size are formed. Thus, the bottom SiN-layer now make up a freely suspended 50 nm SiN square membrane and the wafer is ready for further processing. From this point forward, since the rest of the process is performed on the opposite side of the wafer, the side with the newly formed SiN membranes in the bottom SiN-layer is referred to as "topside" instead.

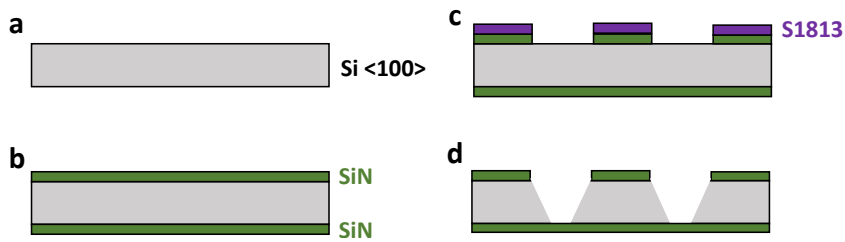

Figure 5.2: Schematic of the membrane fabrication steps, starting with: **a** clean Si-wafer, **b** growing 50 nm SiN with LPCVD, **c** patterning windows in a layer of positive photoresist and **d** anisotropically wet etching the exposed Si with KOH until the bottom SiN is reached.

Next, plasmonic nanopores are created in the topside SiN membrane using

EBL and a lift-off approach. A schematic of the general processing steps can be found in Figure 5.3. First, the wafer with SiN membranes is cleaned using the same RCA2 protocol as used before LPCVD in order to remove surface doped K^+ ions after KOH-etching, since they may damage tools and instrumentation used later on. Following rinsing in acetone and isopropanol in addition to drying using a N_2 stream, a short (2-5 minutes) oven bake is performed to ensure complete removal of organic solvent and an adhesion promotor (Microchemicals Ti-prime) is spin-coated on the topside SiN-layer at 3000 RPM for 20 seconds and baked in an oven at 120° for at least 10 minutes. We have found that this step can be crucial to achieve sufficient adhesion between the adhesion promotor and electron beam resist, in addition to switching to fresh chemicals if adhesion problems arise.

After adhesion layer baking, a negative electron beam resist (Microresist technology ma-N 2403) is spin-coated at 3000 RPM for 60 seconds and a final 10 minute oven bake for curing and improving resist adhesion. A two dimensional 100 x 100 μm^2 grid of 70-140 nm circles with 300 nm pitch is then patterned over a section of each topside membrane using EBL with parameters: 4 nm beam step size, 300 µm aperture, 2 nA beam current and 410 $\mu C/cm^2$ dose. The resist is then developed for 60s using its corresponding developer (Microresist technology ma-D 525) and rinsed immediately in H_2O. The result is a grid of free-standing 300 nm tall pillars at the exposed pattern of circles of *negative* photoresist on the SiN membrane.

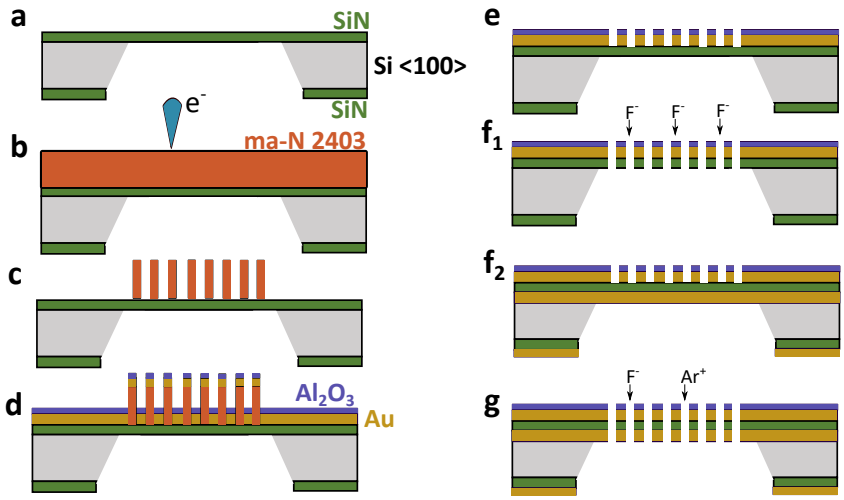

Figure 5.3: Schematic of the nanopore fabrication steps, starting with: **a** a clean Si-wafer with SiN membrane, **b** coating with E-resist and EBL exposure, **c** development of E-resist leaving pillars on the surface, **d** metal deposition using PVD, **e** lift-off in photoresist remover, $\mathbf{f}_1$ removal of SiN using RIE for final nanopore structure, $\mathbf{f}_2$ alternative addition of second metal layer using PVD and **g** removal of SiN and Au using RIE and ion beam milling.

At this point, physical vapour deposition (PVD) is used to cover the whole topside surface in a 1 nm chromium adhesion layer, 30 nm gold layer and a 15 nm aluminium oxide protective layer. The metal covered pillars can then be removed in a lift-off procedure where the wafer is suspended topside-down in a photoresist remover using a custom horisontal teflon dipper under high stirring for 4 hours at 55°, leaving holes in the deposited metal film where the pillars were previously located.

A selection between having a single metal film or metal films on both sides of the membrane can now be made. If only a single film is desired, another RIE step can be performed directly (or after a short 50 W O_2-plasma ash to remove potential resist residues in the pores) to etch away the final exposed SiN layer in the bottom of the holes, resulting in the final nanopore membrane

structure. If a sandwiched membrane structure with two metal films is desired, another PVD step with 1 nm chromium and 30 nm gold is first performed on the bottom side of the wafer. This is then followed by an RIE step on the top side to etch away the SiN layer in the holes until the second gold layer is reached[72]. Since the second gold layer is not sufficiently etched using RIE, a final ion beam milling step is performed to achieve the final nanopore membrane structure. The protective aluminium oxide layer can be readily dissolved in a base (such as 10 mM NaOH) to expose the underlying gold layer if needed.

CHAPTER 6

Concluding Remarks and Future Work

Concluding remarks

The work presented in **Paper 1** on the hydrogen bond complexation process between a polymer brush and a poly(carboxylic acid) on a gold surface revealed that the polymer brush undergoes drastic morphological and rheological changes. The pH reversible collapse in brush height is particularly interesting for its potential to be utilized in a macromolecular gating system driven by small changes in pH. In **Paper 2**, a new plasmonic nanopore array with inherent label-free surface and pore-cavity sensing capabilities is presented. It will play a crucial part as a testing platform for evaluating the macromolecular gating potential of the PEG-PMAA interaction.

Future outlook

In order to see if the height change in the PEG-PMAA system is sufficient to achieve translocation through a blocked nanopore, thorough investigation using plasmonic nanopore arrays together with fluorescence microscopy will be performed. To show a proof of concept of the gating mechanism, suitable model proteins which are stable down to pH 4.5 and can adsorb to the nanopore walls need to be used.

Some preliminary results are shown in Figure 6.1, where liquid-phase atomic force microscopy scans of nanowells functionalised with a 20 kDa PEG brush indicate a larger pore opening as PMAA is adsorbed at low pH compared to after rinsing.

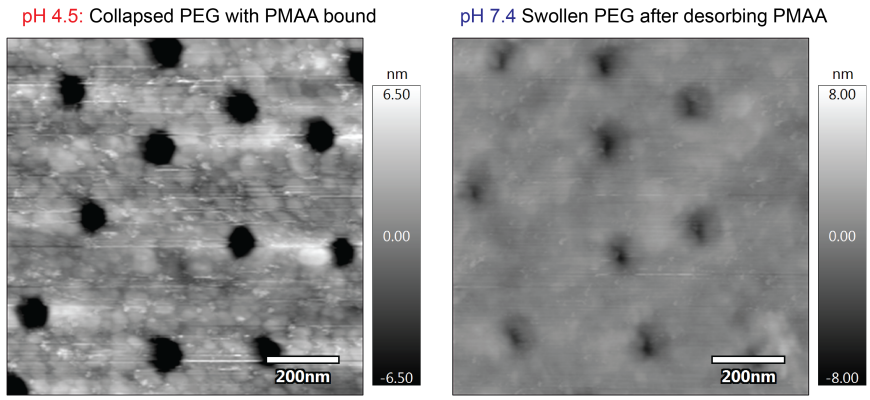

Figure 6.1: Atomic force microscopy images of the PEG-PMAA system utilised on Nanowells. Figure created by Gustav F.D. del Castillo and liquid AFM measurements were performed by Ulrich Ramach at TU Wien.

The PEG-PMAA macromolecular gating system is inherently limited to work for biomolecules that are stable at pH 4.5, which limits the number of different proteins which could be studied. However, this pH range is ideal for studying proteins found in the lysosome, where the pH naturally lies between 4–5 and which hold several types of hydrolytic enzymes. An alternative poly(carboxylic acid) closely related to PMAA known as PEAA (poly(2-ethylacrylic acid) could be a promising candidate for achieving a higher pH_{crit} closer to neutral pH[73], providing a more generally applicable gating approach.

Another enticing concept would be to use electrochemical pH switching with hydroquinone[74] to change the local pH close to the gold surface and induce PEG-PMAA interactions without changing the bulk pH. This would allow usage of any pH above the pH_{crit} and the possibility of directly integrating the gating mechanism with electronic circuitry.

References

[1] T. U. Consortium, "UniProt: a worldwide hub of protein knowledge", *Nucleic Acids Research*, vol. 47, no. D1, pp. D506–D515, 2018.

[2] H. Berman, K. Henrick, H. Nakamura, and J. L. Markley, "The worldwide Protein Data Bank (wwPDB): ensuring a single, uniform archive of PDB data", *Nucleic Acids Research*, vol. 35, no. suppl_1, pp. D301–D303, 2006.

[3] M. Brucale, B. Schuler, and B. Samorì, *Single-molecule studies of intrinsically disordered proteins*, 2014.

[4] V. N. Uversky, C. J. Oldfield, and A. K. Dunker, "Intrinsically Disordered Proteins in Human Diseases: Introducing the D 2 Concept", *Annual Review of Biophysics*, vol. 37, no. 1, pp. 215–246, Jun. 2008.

[5] Y.-L. Ying and Y.-T. Long, "Nanopore-Based Single-Biomolecule Interfaces: From Information to Knowledge", *Journal of the American Chemical Society*, vol. 141, no. 40, pp. 15 720–15 729, Oct. 2019.

[6] L. Schermelleh, A. Ferrand, T. Huser, C. Eggeling, M. Sauer, O. Biehlmaier, and G. P. Drummen, "Super-resolution microscopy demystified", *Nature Cell Biology*, vol. 21, no. 1, pp. 72–84, 2019.

[7] C. Dekker, "Solid-state nanopores", *Nature Nanotechnology*, vol. 2, pp. 209–215, 2007.

[8] O. M. Eggenberger, C. Ying, and M. Mayer, *Surface coatings for solid-state nanopores*, 2019.

[9] S. W. Kowalczyk, L. Kapinos, T. R. Blosser, T. Magalhães, P. Van Nies, R. Y. Lim, and C. Dekker, "Single-molecule transport across an individual biomimetic nuclear pore complex", *Nature Nanotechnology*, vol. 6, no. 7, pp. 433–438, Jun. 2011.

[10] H. Chen, Y. Li, Y. Liu, T. Gong, L. Wang, and S. Zhou, "Highly pH-sensitive polyurethane exhibiting shape memory and drug release", *Polymer Chemistry*, vol. 5, no. 17, pp. 5168–5174, Jul. 2014.

[11] J. S. Suk, Q. Xu, N. Kim, J. Hanes, and L. M. Ensign, *PEGylation as a strategy for improving nanoparticle-based drug and gene delivery*, Apr. 2016.

[12] G. Emilsson, K. Xiong, Y. Sakiyama, B. Malekian, V. Ahlberg Gagnér, R. L. Schoch, R. Y. Lim, and A. B. Dahlin, "Polymer brushes in solid-state nanopores form an impenetrable entropic barrier for proteins", *Nanoscale*, vol. 10, no. 10, pp. 4663–4669, 2018.

[13] G. Emilsson, R. L. Schoch, L. Feuz, F. Höök, R. Y. Lim, and A. B. Dahlin, "Strongly stretched protein resistant poly(ethylene glycol) brushes prepared by grafting-to", *ACS Applied Materials and Interfaces*, vol. 7, no. 14, pp. 7505–7515, 2015.

[14] V. V. Khutoryanskiy and G. Staikos, *Hydrogen-bonded interpolymer complexes: formation, structure and applications*. World Scientific, 2009.

[15] M. Rubinstein and R. Colby, *Polymer physics*. 2003.

[16] G. Fleer, M. A. C. Stuart, J. M. H. M. Scheutjens, T. Cosgrove, and B. Vincent, *Polymers at interfaces*. Springer Science & Business Media, 1993.

[17] R. A. Jones, *Soft condensed matter*, 2002.

[18] P. G. de Gennes, *Polymers at an interface; a simplified view*, Jul. 1987.

[19] S. T. Milner, "Polymer brushes", *Science*, vol. 251, no. 4996, pp. 905–914, 1991.

[20] S. T. Milner, T. A. Witten, and M. E. Cates, "A parabolic density profile for grafted polymers", *EPL*, vol. 5, no. 5, pp. 413–418, 1988.

[21] J. O. Zoppe, N. C. Ataman, P. Mocny, J. Wang, J. Moraes, and H. A. Klok, "Surface-Initiated Controlled Radical Polymerization: State-of-the-Art, Opportunities, and Challenges in Surface and Interface Engineering with Polymer Brushes", *Chemical Reviews*, vol. 117, no. 3, pp. 1105–1318, 2017.

[22] T. Bürgi, "Properties of the gold-sulphur interface: from self-assembled monolayers to clusters", *Nanoscale*, vol. 7, no. 38, pp. 15 553–15 567, 2015.

[23] Y. Xue, X. Li, H. Li, and W. Zhang, "Quantifying thiol-gold interactions towards the efficient strength control", *Nature Communications*, vol. 5, no. 1, pp. 1–9, Jul. 2014.

[24] R. F. Tabor, A. J. Morfa, F. Grieser, D. Y. C. Chan, and R. R. Dagastine, "Effect of gold oxide in measurements of colloidal force", *Langmuir*, vol. 27, no. 10, pp. 6026–6030, May 2011.

[25] U. Wattendorf and H. P. Merkle, "PEGylation as a tool for the biomedical engineering of surface modified microparticles", *Journal of Pharmaceutical Sciences*, vol. 97, no. 11, pp. 4655–4669, Nov. 2008.

[26] B. Ensing, A. Tiwari, M. Tros, J. Hunger, S. R. Domingos, C. Pérez, G. Smits, M. Bonn, D. Bonn, and S. Woutersen, "On the origin of the extremely different solubilities of polyethers in water", *Nature Communications*, vol. 10, no. 1, pp. 1–8, Dec. 2019.

[27] F. Oesterhelt, M. Rief, and H. E. Gaub, "Single molecule force spectroscopy by AFM indicates helical structure of poly(ethylene-glycol) in water", *New Journal of Physics*, vol. 1, no. 1, pp. 6–6, Jan. 1999.

[28] S. Liese, M. Gensler, S. Krysiak, R. Schwarzl, A. Achazi, B. Paulus, T. Hugel, J. P. Rabe, and R. R. Netz, "Hydration Effects Turn a Highly Stretched Polymer from an Entropic into an Energetic Spring", *ACS Nano*, vol. 11, no. 1, pp. 702–712, Jan. 2017.

[29] F. Kienberger, V. P. Pastushenko, G. Kada, H. J. Gruber, C. Riener, H. Schindler, and P. Hinterdorfer, "Static and Dynamical Properties of Single Poly(Ethylene Glycol) Molecules Investigated by Force Spectroscopy", *Single Molecules*, vol. 1, no. 2, pp. 123–128, Jun. 2000.

[30] E. Schneck, A. Schollier, A. Halperin, M. Moulin, M. Haertlein, M. Sferrazza, and G. Fragneto, "Neutron reflectometry elucidates density profiles of deuterated proteins adsorbed onto surfaces displaying poly(ethylene glycol) brushes: Evidence for primary adsorption", *Langmuir*, vol. 29, no. 46, pp. 14 178–14 187, Nov. 2013.

[31] L. Nová, F. Uhlík, and P. Košovan, "Local pH and effective pKA of weak polyelectrolytes-insights from computer simulations", *Physical Chemistry Chemical Physics*, vol. 19, no. 22, pp. 14 376–14 387, Jun. 2017.

[32] R. Arnold, "The titration of polymeric acids", *Journal of Colloid Science*, vol. 12, no. 6, pp. 549–556, Dec. 1957.

[33] T. N. Nekrasova, Y. V. Anufriyeva, A. M. Yel'yashevich, and O. B. Ptitsyn, "Potentiometric titration of polyacrylic acid, polymethacrylic acid and poly-l-glutamic acid", *Polymer Science U.S.S.R.*, vol. 7, no. 5, pp. 1008–1018, Jan. 1965.

[34] R. R. Netz and D. Anderlman, "Neutral and charged polymers at interfaces", *Phys. Rep.-Rev. Sec. Phys. Lett*, vol. 380, pp. 1–95, 2003.

[35] I. Papisov, V. Baranovskii, Y. Sergieva, A. Antipina, and V. Kabanov, "Thermodynamics of complex formation between polymethacrylic and polyacrylic acids and polyethylene glycols. Calculation of temperatures of breakdown of complexes of oligomers and matrices", *Polymer Science U.S.S.R.*, vol. 16, no. 5, pp. 1311–1321, Jan. 1974.

[36] A. Antipina, V. Baranovskii, I. Papisov, and V. Kabanov, "Equilibrium peculiarities in the complexing of polymeric acids with poly (ethylene glycols)", *Polymer Science U.S.S.R.*, vol. 14, no. 4, pp. 1047–1057, Jan. 1972.

[37] Y. Osada and M. Sato, "THERMAL EQUILIBRIUM OF THE INTERMACROMOLECULAR COMPLEXES OF POLYCARBOXYLIC ACIDS REALIZED BY COOPERATIVE HYDROGEN BONDING.", *J Polym Sci Part B Polym Lett*, vol. 14, no. 3, pp. 129–134, Mar. 1976.

[38] Z. Nurkeeva, G. Mun, V. Khutoryanskiy, A. Zotov, and R. Mangazbaeva, "Interpolymer complexes of poly(vinyl ether) of ethylene glycol with poly(carboxylic acids) in aqueous, alcohol and mixed solutions", *Polymer*, vol. 41, no. 21, pp. 7647–7651, Oct. 2000.

[39] T. Ikawa, K. Abe, K. Honda, and E. Tsuchida, "Interpolymer complex between poly(ethylene oxide) and poly(carboxylic acid)", *Journal of Polymer Science: Polymer Chemistry Edition*, vol. 13, no. 7, pp. 1505–1514, Jul. 1975.

[40] J. L. Lutkenhaus, K. D. Hrabak, K. McEnnis, and P. T. Hammond, "Elastomeric flexible free-standing hydrogen-bonded nanoscale assemblies", *Journal of the American Chemical Society*, vol. 127, no. 49, pp. 17 228–17 234, Dec. 2005.

[41] M. Zeghal and L. Auvray, "Structure of polymer complexes in water", *Europhysics Letters*, vol. 45, no. 4, pp. 482–487, Feb. 1999.

[42] H. Raether, *Surface Plasmons on Smooth and Rough Surfaces and on Gratings*. Springer, 1988, vol. 111.

[43] B. Liedberg, C. Nylander, and I. Lunström, "Surface plasmon resonance for gas detection and biosensing", *Sensors and Actuators*, vol. 4, pp. 299–304, Jan. 1983.

[44] L. S. Jung, C. T. Campbell, T. M. Chinowsky, M. N. Mar, and S. S. Yee, "Quantitative Interpretation of the Response of Surface Plasmon Resonance Sensors to Adsorbed Films", *Langmuir*, vol. 14, no. 19, pp. 5636–5648, 1998.

[45] A. B. Dahlin, *Plasmonic Biosensors - An Integrated View of Refractometric Detection*. IOS Press BV, 2012, vol. 4.

[46] J. Vörös, "The density and refractive index of adsorbing protein layers", *Biophysical Journal*, vol. 87, no. 1, pp. 553–561, 2004.

[47] R. L. Schoch and R. Y. H. Lim, "Non-Interacting Molecules as Innate Structural Probes in Surface Plasmon Resonance", *Langmuir*, vol. 29, no. 12, pp. 4068–4076, Mar. 2013.

[48] I. Reviakine, D. Johannsmann, and R. P. Richter, "Hearing what you cannot see and visualizing what you hear: Interpreting quartz crystal microbalance data from solvated interfaces", *Analytical Chemistry*, vol. 83, no. 23, pp. 8838–8848, Dec. 2011.

[49] M. Rodahl, F. Höök, A. Krozer, P. Brzezinski, and B. Kasemo, "Quartz crystal microbalance setup for frequency and Q -factor measurements in gaseous and liquid environments", *Review of Scientific Instruments*, vol. 66, no. 7, pp. 3924–3930, Jul. 1995.

[50] G. Sauerbrey, "Use of quartz vibration for weighing thin films on a microbalance", *Physik J*, 1959.

[51] M. Rodahl and B. Kasemo, "Frequency and dissipation-factor responses to localized liquid deposits on a QCM electrode", *Sensors and Actuators, B: Chemical*, vol. 37, no. 1-2, pp. 111–116, Nov. 1996.

[52] F. Höök, B. Kasemo, T. Nylander, C. Fant, K. Sott, and H. Elwing, "Variations in coupled water, viscoelastic properties, and film thickness of a Mefp-1 protein film during adsorption and cross-linking: A quartz crystal microbalance with dissipation monitoring, ellipsometry, and surface plasmon resonance study", *Analytical Chemistry*, vol. 73, no. 24, pp. 5796–5804, Dec. 2001.

[53] G. Dunér, E. Thormann, and A. Dedinaite, "Quartz Crystal Microbalance with Dissipation (QCM-D) studies of the viscoelastic response from a continuously growing grafted polyelectrolyte layer", *Journal of Colloid and Interface Science*, vol. 408, no. 1, pp. 229–234, Oct. 2013.

[54] M. V. Voinova, M. Rodahl, M. Jonson, and B. Kasemo, "Viscoelastic Acoustic Response of Layered Polymer Films at Fluid-Solid Interfaces: Continuum Mechanics Approach", *Physica Scripta*, vol. 59, no. 5, pp. 391–396, May 1999.

[55] J. N. Israelachvili, "Thin film studies using multiple-beam interferometry", *Journal of Colloid And Interface Science*, vol. 44, no. 2, pp. 259–272, Aug. 1973.

[56] J. N. Israelachvili and G. E. Adams, "Measurement of forces between two mica surfaces in aqueous electrolyte solutions in the range 0-100 nm", *Journal of the Chemical Society, Faraday Transactions 1: Physical Chemistry in Condensed Phases*, vol. 74, no. 0, pp. 975–1001, Jan. 1978.

[57] P. Bilotto, M. Lengauer, J. Andersson, U. Ramach, L. L. Mears, and M. Valtiner, "Interaction Profiles and Stability of Rigid and Polymer-Tethered Lipid Bilayer Models at Highly Charged and Highly Adhesive Contacts", *Langmuir*, vol. 35, no. 48, pp. 15 552–15 563, Dec. 2019.

[58] J. Israelachvili, Y. Min, M. Akbulut, A. Alig, G. Carver, W. Greene, K. Kristiansen, E. Meyer, N. Pesika, K. Rosenberg, and H. Zeng, "Recent advances in the surface forces apparatus (SFA) technique", *Reports on Progress in Physics*, vol. 73, no. 3, p. 16, Jan. 2010.

[59] T. L. Kuhl, D. E. Leckband, D. D. Lasic, and J. N. Israelachvili, "Modulation of interaction forces between bilayers exposing short-chained ethylene oxide headgroups", *Biophysical Journal*, vol. 66, no. 5, pp. 1479–1488, May 1994.

[60] G. Ferrand-Drake Del Castillo, R. L. Hailes, and A. Dahlin, "Large Changes in Protonation of Weak Polyelectrolyte Brushes with Salt Concentration-Implications for Protein Immobilization", *Journal of Physical Chemistry Letters*, vol. 11, no. 13, pp. 5212–5218, Jun. 2020.

[61] J. R. Dorgan, M. Stamm, and C. Toprakcioglu, "Adsorption kinetics of end-attaching triblock copolymers", *Polymer*, vol. 34, no. 7, pp. 1554–1557, Jan. 1993.

[62] C.-J. Huang, L.-C. Wang, C.-Y. Liu, A. S. T. Chiang, and Y.-C. Chang, "Natural zwitterionic organosulfurs as surface ligands for antifouling and responsive properties", *Biointerphases*, vol. 9, no. 2, p. 029 010, Jun. 2014.

[63] A. Saftics, G. A. Prósz, B. Türk, B. Peter, S. Kurunczi, and R. Horvath, "In situ viscoelastic properties and chain conformations of heavily hydrated carboxymethyl dextran layers: a comparative study using OWLS and QCM-I chips coated with waveguide material", *Scientific Reports*, vol. 8, no. 1, pp. 1–14, Dec. 2018.

[64] P. González-Tello, F. Camacho, and G. Blázquez, "Density and Viscosity of Concentrated Aqueous Solutions of Polyethylene Glycol", *Journal of Chemical and Engineering Data*, vol. 39, no. 3, pp. 611–614, 1994.

[65] D. V. Verschueren, S. Pud, X. Shi, L. De Angelis, L. Kuipers, and C. Dekker, "Label-Free Optical Detection of DNA Translocations through Plasmonic Nanopores", *ACS Nano*, vol. 13, no. 1, pp. 61–70, Jan. 2019.

[66] J. D. Spitzberg, A. Zrehen, X. F. van Kooten, and A. Meller, "Plasmonic-Nanopore Biosensors for Superior Single-Molecule Detection", *Advanced Materials*, p. 1 900 422, Apr. 2019.

[67] A. B. Dahlin, *Sensing applications based on plasmonic nanopores: The hole story*, 2015.

[68] B. Malekian, K. Xiong, G. Emilsson, J. Andersson, C. Fager, E. Olsson, E. M. Larsson-Langhammer, and A. B. Dahlin, "Fabrication and characterization of plasmonic nanopores with cavities in the solid support", *Sensors (Switzerland)*, 2017.

[69] T. Sannomiya, O. Scholder, K. Jefimovs, C. Hafner, and A. B. Dahlin, "Investigation of plasmon resonances in metal films with nanohole arrays for biosensing applications", *Small*, 2011.

[70] J. Prikulis, P. Hanarp, L. Olofsson, D. Sutherland, and M. Käll, "Optical spectroscopy of nanometric holes in thin gold films", *Nano Letters*, vol. 4, no. 6, pp. 1003–1007, Jun. 2004.

[71] E. S. H. Kang, H. Ekinge, and M. P. Jonsson, "Plasmonic fanoholes: on the gradual transition from suppressed to enhanced optical transmission through nanohole arrays in metal films of increasing film thickness", *Optical Materials Express*, vol. 9, no. 3, p. 1404, Mar. 2019.

[72] A. B. Dahlin, M. Mapar, K. Xiong, F. Mazzotta, F. Höök, T. Sannomiya, F. Höök, and T. Sannomiya, "Plasmonic Nanopores in Metal-Insulator-Metal Films", *Advanced Optical Materials*, vol. 2, no. 6, pp. 556–564, Jun. 2014.

[73] Y. Lu, A. Zhuk, L. Xu, X. Liang, E. Kharlampieva, and S. A. Sukhishvili, "Tunable pH and temperature response of weak polyelectrolyte brushes: Role of hydrogen bonding and monomer hydrophobicity", *Soft Matter*, vol. 9, no. 22, pp. 5464–5472, May 2013.

[74] W. Yi, C. Ji, J. Fei, and X. He, "Reversible Switched pH-Responsive Hydroquinone Electrochemical Sensor Based on Composite Film of Polystyrene-b-Poly (Acrylic Acid) and Graphene Oxide", *Electroanalysis*, vol. 30, no. 12, pp. 2888–2898, Dec. 2018.